

Towards Accurate Modelling of Galaxy Clustering on Small Scales: Testing the Standard Λ CDM + Halo Model

Manodeep Sinha^{1,2,6*}, Andreas A. Berlind¹, Cameron K. McBride³,
Roman Scoccimarro⁴, Jennifer A. Piscionere^{1,2}, & Benjamin D. Wibking^{1,5}

¹*Department of Physics and Astronomy, Vanderbilt University, Nashville, TN 37235, USA*

²*Centre for Astrophysics & Supercomputing, Swinburne University of Technology, 1 Alfred St., Hawthorn, VIC 3122, Australia*

³*Harvard-Smithsonian Center for Astrophysics, 60 Garden St., Cambridge, MA 02138*

⁴*Center for Cosmology and Particle Physics, New York University, New York, NY 10003*

⁵*Department of Astronomy, The Ohio State University, Columbus, OH 43210*

⁶*ARC Centre of Excellence for All Sky Astrophysics in 3 Dimensions (ASTRO 3D)*

Accepted XXX. Received YYY; in original form ZZZ

ABSTRACT

Interpreting the small-scale clustering of galaxies with halo models can elucidate the connection between galaxies and dark matter halos. Unfortunately, the modelling is typically not sufficiently accurate for ruling out models statistically. It is thus difficult to use the information encoded in small scales to test cosmological models or probe subtle features of the galaxy-halo connection. In this paper, we attempt to push halo modelling into the “accurate” regime with a fully numerical mock-based methodology and careful treatment of statistical and systematic errors. With our forward-modelling approach, we can incorporate clustering statistics beyond the traditional two-point statistics. We use this modelling methodology to test the standard Λ CDM + halo model against the clustering of SDSS DR7 galaxies. Specifically, we use the projected correlation function, group multiplicity function and galaxy number density as constraints. We find that while the model fits each statistic separately, it struggles to fit them simultaneously. Adding group statistics leads to a more stringent test of the model and significantly tighter constraints on model parameters. We explore the impact of varying the adopted halo definition and cosmological model and find that changing the cosmology makes a significant difference. The most successful model we tried (Planck cosmology with Mvir halos) matches the clustering of low luminosity galaxies, but exhibits a 2.3σ tension with the clustering of luminous galaxies, thus providing evidence that the “standard” halo model needs to be extended. This work opens the door to adding interesting freedom to the halo model and including additional clustering statistics as constraints.

Key words: cosmology: theory — cosmology: dark matter — cosmology: large-scale structure of Universe — galaxies: evolution — galaxies: halos — galaxies: groups: general — methods: numerical

1 INTRODUCTION

The observed spatial distribution of galaxies contains a richness of information about the initial conditions and subsequent evolution of the matter density field in the universe. Moreover, the dependence of the spatial distribution of galaxies on their observed properties contains information about the physics of galaxy formation and evolution. The study of galaxy clustering has thus proved to be a fruit-

ful avenue for constraining cosmology and galaxy formation theory and it has provided the primary motivation for the construction of large astronomical galaxy surveys.

The specific information content of galaxy clustering depends on the physical scales considered. On large scales, galaxy clustering provides fairly clean constraints on cosmology because galaxies are simple tracers of the matter density field (e.g., Scherrer & Weinberg 1998; Narayanan et al. 2000). Prime examples of such constraints are measurements of the large-scale galaxy power spectrum (e.g., Tegmark et al. 2004) and the Baryon Acoustic Oscillation

* E-mail: msinha@swin.edu.au

(BAO) signature (Eisenstein et al. 2005). On small scales ($\lesssim 10h^{-1}\text{Mpc}$), galaxy clustering depends both on cosmology and on the detailed relationship between the galaxy and dark matter density fields, i.e., the *bias*, which is nontrivial and is set by the physics of galaxy formation. Although in principle galaxy clustering measurements on small scales have the potential to constrain both cosmological and galaxy formation theories, in practice this is extremely challenging because the process of galaxy formation is very complex and we currently lack a complete predictive theory for it. Moreover, the most accurate theories that do exist require computationally expensive hydrodynamic simulations to make predictions, and are thus not suited for exploring and constraining large parameter spaces.

Halo based models that begin with the assumption that galaxies form and live inside dark matter halos provided the breakthrough that made it possible to quantitatively model galaxy clustering on small scales. These models rely on the fact that the statistical properties of dark matter halos are easy to predict with collision-less N-body simulations where the only important physical process is gravity. Halo models then adopt a parameterisation to connect galaxies to halos, thus bypassing the need to understand galaxy formation physics. In the halo model framework, there is a convenient conceptual and operational division between the roles of cosmology and galaxy formation: cosmology dictates the dark matter halo distribution while galaxy formation determines how exactly galaxies occupy halos. This division is not perfect since gas physics can affect the properties of halos (e.g., Cui et al. 2012); however, this is a second order effect.

The connection between galaxy halo occupation and galaxy clustering was first made by semi-analytic models of galaxy formation that modelled the formation and evolution of galaxies inside halos. Since these halos resided within a larger density field in cosmological N-body simulations, it was straightforward to predict the clustering of the semi-analytic galaxies (Kauffmann et al. 1997, 1999; Baugh et al. 1999). Jing et al. (1998) and Benson et al. (2000) took this a step further by realising that galaxy clustering did not necessarily depend on all the details of galaxy formation, but rather only cared about halo occupation statistics as a function of halo mass. A series of papers then built upon the earlier work of Neyman & Scott (1952) and Scherrer & Bertschinger (1991) to develop a full analytic machinery for combining parameterised halo properties with occupation statistics to calculate the correlation function and power spectrum of galaxies on all scales (e.g., Peacock & Smith 2000; Seljak 2000; Scoccimarro et al. 2001; Cooray & Sheth 2002). These analytic models became generally known as the “halo model”. Berlind & Weinberg (2002) focused on the “halo occupation distribution” (HOD), which is the complete parameterisation connecting galaxies of a given class to halos, and they investigated how the HOD affects several galaxy clustering statistics and laid out a road-map for empirically constraining the HOD with measurements of galaxy clustering using data from large surveys.

The halo model has since been used by a large number of studies to model galaxy clustering data in several galaxy redshift surveys: the 2dF Galaxy Redshift Survey (2dFGRS; Colless et al. 2001), the Sloan Digital Sky Survey (SDSS; York et al. 2000), the 6dF Galaxy Redshift Survey (6dFGRS; Jones et al. 2004), and the SDSS III Baryon Os-

cillation Spectroscopic Survey (BOSS; Dawson et al. 2013). Some studies investigated the two-point correlation function of low redshift galaxies (Magliocchetti & Porciani 2003; Zehavi et al. 2004; Collister & Lahav 2005; Zehavi et al. 2005; Tinker et al. 2005; Zehavi et al. 2011; Watson et al. 2012; Beutler et al. 2013; Piscionere et al. 2015), others investigated the same for red galaxies (Blake et al. 2008; Brown et al. 2008; Zheng et al. 2009; Watson et al. 2010; White et al. 2011; Parejko et al. 2013; Nikoloudakis et al. 2013; Guo et al. 2014; Reid et al. 2015; Guo et al. 2015a), or other special classes of galaxies such as AGN or radio galaxies (Wake et al. 2008; Mandelbaum et al. 2009; Richardson et al. 2013). Many studies modelled the two-point correlation function of Lyman Break and other types of high redshift galaxies (Bullock et al. 2002; Moustakas & Somerville 2002; Hamana et al. 2004; Zheng 2004; Lee et al. 2006; Tinker et al. 2010; Jose et al. 2013; Kim et al. 2014), while others combined modelling of galaxies at different redshifts in order to learn about the co-evolution of galaxies and halos (Yan et al. 2003; Cooray 2006; Zheng et al. 2007; Tinker & Wetzel 2010; Abbas et al. 2010; Wake et al. 2011; Tinker et al. 2013). Though the vast majority of studies have focused on the two-point correlation function, a few have applied the halo model to other clustering statistics, like the three-point correlation function (Marín 2011), or the galaxy-mass cross-correlation function as measured by galaxy-galaxy lensing (Guzik & Seljak 2002; Cacciato et al. 2013). Closely related to the HOD approach is the conditional luminosity function (CLF) approach that includes galaxy luminosity in the halo occupation parameterisation (e.g., Yang et al. 2003; van den Bosch et al. 2003; Vale & Ostriker 2004; Leauthaud et al. 2011, 2012).

All of these studies successfully used the halo model to translate clustering statistics into constraints on the relation between galaxy properties and the dark matter halos they inhabit. For the most part, the constraints are focused on the relation between the luminosity or stellar mass of galaxies and the mass of their halos (e.g., Zehavi et al. 2011). However, some studies focused on other aspects of the HOD, such as the radial distribution of galaxies within halos (e.g., Watson et al. 2010, 2012; Piscionere et al. 2015), the velocity distribution of galaxies within halos (Guo et al. 2015a,b,c), or galaxy assembly bias (Zentner et al. 2016). These results have been quite illuminating and have helped to explain many observed features of the galaxy population, such as the morphology-density relation and the different clustering strengths of different galaxy types. Halo modelling across different redshifts has even constrained the competing roles of merging and star formation in the stellar mass buildup of galaxies (e.g., Tinker et al. 2013).

In most halo model analyses, the statistical methodology employed is sophisticated. Clustering uncertainties and their correlations are quantified in estimated covariance matrices, parameter searches are executed using Monte Carlo Markov Chain (MCMC) methods, model parameter values are reported with their full probability distributions, and the goodness of fit for the halo model is typically reported using the χ^2 statistic. However, the systematic errors in these analyses have been largely unquantified. Systematic errors exist in the estimation of covariance matrices that typically use the Jackknife method (Norberg et al. 2009). Systematic errors also exist in the halo model itself, since its imple-

mentation is almost always analytic and it contains several approximations. Without a robust characterisation of systematic errors, it is impossible to interpret the published results in a statistical sense. For example, many of the published works contain model fits with reported values of χ^2 that are high enough to warrant ruling the models out (e.g., some of the high luminosity samples in Zehavi et al. 2011), but without a proper accounting of systematic errors in the modelling, it is not possible to determine whether the models have actually been ruled out. This problem is exacerbated by the ever shrinking statistical errors in clustering measurements due to the growing sample sizes provided by current galaxy surveys. In order to trust the goodness of fit reported by a given study, systematic errors in the modelling must be kept smaller than the statistical errors in the data measurements.

Since systematic errors in modelling are for the most part not quantified by published studies, many of the results in the literature should be interpreted with caution. In general, qualitative trends found are likely correct, but precise parameter values, error bars, or goodness of fit estimates are not necessarily reliable. This does not pose a problem for most published works because their goal was to uncover general trends rather than to test specific models. However, if we wish to use the halo model to probe more subtle features of the HOD, like the presence of assembly bias (e.g., see Zentner et al. 2014), or if we wish to use galaxy clustering on small scales to constrain cosmological models, we will need to make our modelling methodology more accurate. A few studies have demonstrated the power of small scales to constrain cosmology (e.g., Abazajian et al. 2005; van den Bosch et al. 2007; Cacciato et al. 2013), but they will only be able to compete with more established probes of cosmology if the modelling is sufficiently accurate.

In this paper, we attempt to push the modelling of galaxy clustering on small scales into the “accurate regime”, where results can be trusted enough to confirm or rule out physical models. To be precise, by “accurate” we mean that *given a set of measured statistics from a galaxy survey, and a galaxy-halo connection model being tested*, we can produce a reliable goodness of fit *and* reliable posterior probabilities for the model parameters. To achieve this, we need to: i) minimize the theoretical errors in the predicted distribution of halos for the assumed cosmological model, ii) forward-model the measured clustering statistics to incorporate all observational systematic errors, and iii) robustly estimate the statistical errors and covariances in the measured clustering statistics *from the model*. In other words, our goal is to accomplish for small scales what is already routinely done in the study of large scale clustering. This is an ambitious goal and we can only tackle it by adopting a fully numerical modelling framework that is based on large numbers of realistic mock galaxy catalogues. This data-intensive approach requires substantial computational effort. However, we are motivated to do this by the immense amount of information present in galaxy surveys on small scales, which is currently not being harnessed. In this first paper, we primarily assume that the cosmological model is known and we adopt the most widely used formulation of the HOD to model the clustering of SDSS galaxies. Our objective is thus to test the standard Λ CDM + halo model against the small scale clustering of SDSS galaxies. Specifically, we use measurements of

the projected correlation function and the group multiplicity function for two luminosity threshold samples from the SDSS DR7 (Abazajian et al. 2009) dataset. However, this work is also intended to open the door for future studies where we will use additional clustering statistics and larger galaxy samples to test extensions of the standard HOD as well as variations in cosmology.

The layout of this paper is as follows. In § 2 we describe the SDSS data samples that we use. In § 3 we describe the N-body simulations and mock galaxy catalogues that make up the workhorse of our modelling methodology. In § 4 we present our galaxy clustering measurements and in § 5 we present their associated errors and correlation matrices. In § 6 we describe our model fitting methodology and present all of our modelling results. In § 7 we discuss future improvements to our methodology. Finally, in § 8 we summarise our results.

2 SDSS GALAXY SAMPLES

The Sloan Digital Sky Survey (York et al. 2000) completed its original imaging and spectroscopic goals in 2008 with its seventh data release (DR7; Abazajian et al. 2009). The DR7 spectroscopic main galaxy sample (Strauss et al. 2002) is complete down to an apparent r -band Petrosian magnitude limit of 17.77 and contains over 900,000 galaxies. In this work, we use the large-scale structure samples from the NYU Value Added Galaxy Catalog (NYU-VAGC; Blanton et al. 2005). Specifically, we use a parent sample of just over 530,000 galaxies, which only covers the northern part of the SDSS footprint and is cut back to $r < 17.6$ so that it is complete down to that magnitude limit across the sky. The reason for restricting the data to the northern footprint is that we can construct more independent mock catalogues using the north-only survey volume. Galaxy absolute magnitudes have been k -corrected to rest-frame magnitudes at redshift $z = 0.1$ (Blanton et al. 2003b) and corrected for passive luminosity evolution using the simple model described by Blanton (2006).

The SDSS spectroscopic sample has an incompleteness due to the mechanical restriction that spectroscopic fibres cannot be placed closer to each other than their own thickness. This fibre collision constraint makes it impossible to obtain redshifts for both galaxies in pairs that are closer than $55''$ on the sky. This restriction results in $\sim 7\%$ of targeted galaxies not having a measured redshift. We assign fibre collided galaxies the redshift of the galaxy they collided with (i.e., the “nearest neighbour correction”; Zehavi et al. 2002). This correction recovers the true correlation function well on scales larger than the physical scale corresponding to $55''$, which for the outer redshift limit of our samples corresponds to $0.1h^{-1}$ Mpc. There is some additional incompleteness due to bright foreground stars blocking background galaxies, but this is at the 1% level.

In this study we use two volume-limited subsamples of the full SDSS redshift sample that are each complete in a specified redshift range down to a limiting r -band absolute magnitude threshold. We construct each sample by choosing redshift limits z_{\min} and z_{\max} and only keeping galaxies whose evolved, redshifted spectra would still make the redshift survey’s apparent magnitude and surface brightness

Table 1. SDSS Volume-limited Sample Parameters. The first column lists the absolute magnitude threshold of each sample at $z = 0.1$. The second, third and fourth columns list the minimum, maximum and the median redshifts, respectively. The fifth column lists the effective volume of each sample, and the last column lists the galaxy number density.

M_r^{lim}	z_{min}	z_{max}	z_{median}	V_{eff} $10^6 h^{-3} \text{Mpc}^3$	n_g $h^3 \text{Mpc}^{-3}$
-19	0.02	0.067	0.054	5.555	0.0149
-21	0.02	0.165	0.132	78.374	0.0012

cuts at these limiting redshifts. Our low-luminosity sample is complete down to an r -band absolute magnitude of -19 in the redshift range $0.02 - 0.067$, while our high-luminosity sample is complete down to an r -band absolute magnitude of -21 in the redshift range $0.02 - 0.165$. The redshift limits, median redshift, effective volume, and number density of these two samples are listed in Table 1. The volumes and number densities of the samples are corrected for survey incompleteness.

Throughout this paper, co-moving distances and absolute magnitudes for SDSS galaxies are calculated adopting a flat Λ CDM cosmological model with $\Omega_m = 0.25$ and $h = 1$. Our distances thus have units of $h^{-1} \text{Mpc}$ and our absolute magnitudes are actually $M_r + 5 \log h$. We keep these data samples fixed regardless of what cosmological model we adopt when fitting to clustering statistics. Ideally, a change of cosmology in the model should also be reflected in the data measurements. However, we have checked that clustering statistics only change by $\sim 1\%$ when switching cosmological models, which is negligible compared to the errors in our measurements.

3 MOCK GALAXY CATALOGUES

The key to accurate forward halo modelling of galaxy clustering on small scales is to use mock catalogues both for predicting observed statistics and for estimating errors and covariances. Broadly, we can divide the challenge in creating an accurate model into three distinct pieces – 1) creating a reliable prediction of the halo population for a cosmological model, 2) comparing identical galaxy clustering statistics between the predicted model and the observed data 3) correctly estimating covariances between all clustering statistics from the model. We take the following approach to ensure that systematic errors in the modelling are sub-dominant compared to observational errors, i.e., an accurate model. To obtain a reliable halo population, we use cosmological N-body simulations of sufficient volume and resolution. To compare identical clustering statistics, we create realistic mock catalogues (from the N-body simulations) that include systematic effects like survey geometry and redshift-space distortions. In addition, we use the exact same codes, when necessary, to measure the clustering statistics on both mock galaxies and observed data. To correctly estimate covariances, we use a large, independent ensemble of these realistic mocks instead of estimating errors from the observed dataset. Skipping any one of these three steps compromises the “accurate” part of the model. For instance, assuming

an universal halo mass function, or an analytic non-linear bias fitting formula, or a Navarro-Frenk-White density profile for the halo has an impact on the predicted $w_p(r_p)$. Not including survey geometry in the modelling changes both the amplitude and the slope of the group multiplicity function (Berlind et al. 2006). Using jack-knife resampling to build covariance matrices introduces scale-dependent, systematic biases (Norberg et al. 2009). With our adopted methodology, we avoid all these systematic effects and push the small-scale modelling towards the accurate regime.

In this section we describe the simulations and mock catalogue pipeline in detail.

3.1 N-body Simulations and Halo Catalogues

3.1.1 For building covariance matrices

The bulk of simulations that we use are from the Large Suite of Dark Matter Simulations project (LasDamas; McBride et al. 2009). The LasDamas project focused on running many independent N-body realisations with the same cosmology but different initial phases. The cosmological parameters were roughly motivated by the WMAP3 constraints (Spergel et al. 2007) and are $\Omega_m = 0.25$, $\Omega_\Lambda = 0.75$, $\Omega_b = 0.04$, $h = 0.7$, $\sigma_8 = 0.8$, and $n_s = 1.0$. The LasDamas simulations were designed to model SDSS galaxies and consist of four different volume and resolution configurations that correspond to different luminosity samples. In this work, we use the Consuelo and Carmen configurations, which were designed to model galaxy samples with r -band absolute magnitude thresholds of -19 and -21 , respectively.

All the simulations were seeded with second order Lagrangian perturbation theory initial conditions using the code 2LPTIC (Scoccimarro 1998; Crocce et al. 2006) and were evolved using the N-body code GADGET-2 (Springel 2005). Each Consuelo simulation evolved 1400^3 dark matter particles in a cubic volume of $420h^{-1} \text{Mpc}$ on a side, from a starting redshift of $z_{\text{init}} = 99$ to $z = 0$, with a gravitational force softening length of $8h^{-1} \text{kpc}$. Each Carmen simulation evolved 1120^3 dark matter particles in a cubic volume of $1000h^{-1} \text{Mpc}$ on a side, from a starting redshift of $z_{\text{init}} = 49$ to $z = 0$, with a gravitational force softening length of $25h^{-1} \text{kpc}$. The resulting particle masses of the Consuelo and Carmen simulations are $1.87 \times 10^9 h^{-1} M_\odot$ and $4.938 \times 10^{10} h^{-1} M_\odot$, respectively. For the purpose of estimating covariance matrices, we use 50 realisations of each of these two boxes, which yield 200 mock catalogues per luminosity sample.

We identify halos in the dark matter distributions using the simulation outputs corresponding to the median redshifts of the -19 and -21 samples, which are $z = 0.054$ and $z = 0.132$, respectively. For the fifty Consuelo and fifty Carmen simulations, halos were identified with the `ntropy-fofsv` code (Gardner et al. 2007), which employs a friends-of-friends (FoF; Davis et al. 1985) algorithm. The FoF linking length was chosen to be 0.2 times the mean inter-particle separation. Finally, we apply the Warren et al. (2006) correction to the FoF halo masses. For the purpose of placing central galaxies in halos, we define the FoF halo centre to be at the location of the deepest part of the halo’s gravitational potential well. The mock catalogues that we

use to construct covariance matrices are based on these FoF halo catalogues.

The mass resolutions of these simulations result in 150 particles in halos of mass $\log M = 11.45$ (for Consuelo) and 122 particles in halos of mass $\log M = 12.78$ (for Carmen) which, according to Zehavi et al. (2011), are the typical minimum masses we expect to host galaxies in our two luminosity samples. If we also consider the scatter in these minimum masses (the $\sigma_{\log M}$ parameter in Zehavi et al. 2011), then halos with masses as low as $\log M = 11.26$ (for Consuelo) and $\log M = 12.10$ (for Carmen) will sometimes host a galaxy, which contain 97 and 25 particles, respectively. This is acceptable resolution for our purposes because these halos only rarely host a single central galaxy and so we only need to roughly resolve their bulk properties (position, velocity, mass). Moreover, we expect that errors due to resolution will not impact the scatter among clustering measurements from different simulation realisations as much as it will impact the clustering measurements themselves.

3.1.2 For MCMC parameter exploration

For the purpose of generating predictions of clustering statistics within our MCMC framework, we have run a few additional simulations. The demands on simulation resolution are more stringent in this case because, during the halo model parameter search, sometimes galaxies are placed in significantly lower mass halos than they are in the fiducial model that we use to construct covariance matrices. The simulations used in the MCMC parameter search must therefore resolve halos down to lower masses. If we adopt the $2\text{-}\sigma$ low value of $\log M_{\min}$ and $2\text{-}\sigma$ high value of $\sigma_{\log M}$ found by Zehavi et al. (2011), we can obtain a conservative estimate of the lowest mass halos we must resolve. These masses are $\log M = 10.9$ and 11.6 for the -19 and -21 samples, which result in 42 and 8 particles in Consuelo and Carmen simulations, respectively. The Carmen simulations do not therefore have adequate resolution to serve as the basis for modelling the clustering of the $M_r < -21$ SDSS sample. We have thus run a higher resolution version of Carmen that we name CarmenHD, which contains 2240^3 particles and resolves halos that have more than five times smaller mass than Carmen. In order to probe a variation in cosmology, we have also run new versions of Consuelo and CarmenHD that adopt the recent set of cosmological parameters given by the Planck experiment (Planck Collaboration et al. 2014). Specifically, these simulations, named Consuelo-plk and CarmenHD-plk, adopt the following parameter values: $\Omega_m = 0.302$, $\Omega_\Lambda = 0.698$, $\Omega_b = 0.048$, $h = 0.681$, $\sigma_8 = 0.828$, and $n_s = 0.96$. We have run two realisations each of CarmenHD, Consuelo-plk, and CarmenHD-plk since we use two boxes within our MCMC modelling framework. The box sizes, particle masses, force resolutions and other summary information of all the simulations described above are listed in Table 2.

For the two Consuelo, CarmenHD, Consuelo-plk, and CarmenHD-plk simulations that we use in our MCMC modelling, halos are identified with a spherical over-density (SO; Lacey & Cole 1994) algorithm using the ROCKSTAR code (Behroozi et al. 2013). We use two sets of SO halo definitions: the M200b definition where halos are spheres of density 200 times the mean density of the universe and the Mvir

definition where halos have a density that depends on cosmology and redshift, as given by Bryan & Norman (1998). We use these SO halo catalogues to predict galaxy clustering within our MCMC parameter searches. In the case of an SO halo, the halo centre is by definition at the centre of the halo sphere¹

When evaluating the likelihood function during a model parameter exploration, it is desirable that the statistical errors in the model (due to cosmic variance) are much smaller than the errors in the SDSS data so that they do not add appreciably to the error budget. If this is not the case, it is equivalent to degrading the statistical power of the galaxy survey. Therefore, the clustering statistics calculated from the model should come from a larger volume of mock galaxies than the SDSS sample being modelled. On the other hand, generating too large a mock volume on the fly within a MCMC parameter search is computationally intractable. We achieve this balance by using either a single realisation simulation cube in our modelling, or two realisations if it is necessary to faithfully reproduce the SDSS sample geometry. A single Consuelo or Carmen box contains about 13 times more total volume than the SDSS -19 or -21 samples, respectively. Alternatively, if we need to include the full SDSS sample geometry in the mocks, two Consuelo or Carmen boxes can generate eight times more mock volume than their respective SDSS samples. This is sufficiently large to keep statistical errors in the modelling sub-dominant. However, we reduce the model errors further by carefully selecting the two simulation boxes we use. We do this by selecting the two boxes that exhibit a clustering signal closest to the mean of all 50 boxes. We do this in the following way. First, we populate all 50 Consuelo and Carmen boxes with the Zehavi et al. (2011) HOD model for -19 and -20 threshold samples, respectively. We then measure the projected correlation function $w_p(r_p)$ on each of these mocks, adopting one of the axes of the cube as the line-of-sight direction. We measure the mean clustering $\overline{w_p}(r_p)$ from all 50 boxes as well as their standard deviation $\sigma_{w_p}(r_p)$. We then compute a χ^2 statistic for each box

$$\chi_{\text{box}}^2 = \sum_{r_p} \left(\frac{w_{p,\text{box}}(r_p) - \overline{w_p}(r_p)}{\sigma_{w_p}(r_p)} \right)^2, \quad \forall \text{box} \in [1, 50]. \quad (1)$$

Finally, we identify the two realisations of Consuelo and Carmen that have the lowest values of χ^2 , which are essentially the two boxes whose random phases result in clustering that is closest to the mean of all 50 boxes. We use these same exact phases in all our modelling boxes: the same two sets of phases for the two Consuelo and two Consuelo-plk simulations and the same two sets of phases for the two CarmenHD and two CarmenHD-plk simulations. This procedure results in a significant reduction in cosmic variance errors. The average box-to-box scatter in $w_p(r_p)$ across all scales is $\sim 10\%$ for Consuelo and $\sim 6\%$ for Carmen, while the average difference between our best two boxes and the mean of all 50 is

¹ We note that the correlation matrices are derived from FoF halos, while the modelling is done with SO halos. This is because we did not have the SO halo catalogs for all the simulations while the paper was being prepared. We have since checked that our results do not change qualitatively with a correlation matrix derived from SO halos

Table 2. Simulation parameters. The table lists the properties of the simulations used to estimate covariance matrices and to model clustering statistics in our MCMC chains for our two luminosity samples. Columns 3-9 list the cosmological model, simulation name, box size, number of particles, particle mass, force resolution, and number of boxes used.

Use Type	Sample	Cosmology	Simulation	L_{box} $h^{-1}\text{Mpc}$	N_{part}	m_{part} $h^{-1}M_{\odot}$	ϵ $h^{-1}\text{kpc}$	Number
Correlation matrix	-19	LasDamas	Consuelo	420	1400 ³	1.87×10^9	8	50
	-21	LasDamas	Carmen	1000	1120 ³	4.94×10^{10}	25	50
MCMC	-19	LasDamas	Consuelo	420	1400 ³	1.87×10^9	8	2
	-21	LasDamas	CarmenHD	1000	2240 ³	6.17×10^9	12	2
	-19	Planck	Consuelo-plk	420	1400 ³	2.26×10^9	8	2
	-21	Planck	CarmenHD-plk	1000	2240 ³	7.46×10^9	12	2

only $\sim 5\%$ for Consuelo and $\sim 3\%$ for Carmen, representing a factor of two reduction in cosmic variance errors. This is the accuracy we would normally obtain with a much larger simulation volume.

3.2 From Halos to Galaxies

We populate dark matter halos in our simulations with mock galaxies using the ‘Halo Occupation Distribution’ (HOD) framework. In this framework, the number, positions, and velocities of galaxies within a halo are described statistically given a set of parameterised prescriptions. The key advantage of the HOD approach is that if the parameterisation is sufficiently flexible it allows us to marginalise over the full uncertainty of galaxy formation theory.

In this work, we adopt the ‘vanilla’ HOD model of Zheng et al. (2007), which has become somewhat of an industry standard in HOD modelling. Motivated by theoretical results (Kravtsov et al. 2004; Zheng et al. 2005), we split the galaxies into centrals and satellites within their halos. The mean number of central galaxies as a function of halo mass M is given by²

$$\langle N_{\text{cen}} \rangle = \frac{1}{2} \left[1 + \text{erf} \left(\frac{\log M - \log M_{\text{min}}}{\sigma_{\log M}} \right) \right], \quad (2)$$

where M_{min} sets the minimum halo mass that can host a central galaxy, $\sigma_{\log M}$ sets the scatter around this minimum halo mass, and $\text{erf}(x)$ is the error function, $\text{erf}(x) = \frac{2}{\sqrt{\pi}} \int_0^x \exp(-y^2) dy$. The motivation behind this particular analytic form of $\langle N_{\text{cen}} \rangle$ comes from assuming a log-normal distribution of central galaxy luminosity at fixed halo mass. If the luminosity-mass relation is a power law $L \propto M^p$ with a log-normal scatter $\sigma_{\log L}$, then the scatter in mass at fixed luminosity is $\sigma_{\log M} = \sqrt{2} \sigma_{\log L} / p$. The parameter $\sigma_{\log M}$ in equation (2) represents this scatter at the luminosity limit of the sample and thus controls how quickly the probability of containing a galaxy above the luminosity limit rises from zero to one as halo mass increases. M_{min} is the mass at which this probability is one half, i.e., where half the halos in the universe contain a central galaxy above the sample luminosity threshold, while the other half do not. The relation between central galaxy luminosity and halo mass is constrained by abundances to follow a roughly double

power-law form with a steep slope at low mass, a transition near $M = 10^{12} h^{-1} M_{\odot}$, and a shallow slope at high mass (e.g., Vale & Ostriker 2004). For the -19 and -21 luminosity thresholds we consider in this paper, we expect the slope p to be approximately ~ 1 and ~ 0.3 , respectively. Previous work on satellite kinematics has constrained $\sigma_{\log L}$ to be approximately ~ 0.15 dex (More et al. 2009). We thus expect values of $\sigma_{\log M}$ that are ~ 0.2 and ~ 0.7 for our faint and bright samples, respectively.

In each halo we place a number of satellite galaxies drawn from a Poisson³ distribution with a mean given by

$$\langle N_{\text{sat}} \rangle = \langle N_{\text{cen}} \rangle \times \left(\frac{M - M_0}{M_1} \right)^{\alpha}, \quad (3)$$

where M_0 is the halo mass below which there are no satellite galaxies, α is the slope of the power-law occupation function at high masses, and M_1 sets the mass scale where halos contain one satellite galaxy on average. The actual halo mass for which $\langle N_{\text{sat}} \rangle = 1$ is slightly higher than M_1 and also depends on the other parameter values. For some HOD parameter combinations, it is possible to have halos that do not receive a central galaxy and yet still have a chance to get a satellite. We do not allow such cases in our modelling. Halos are only eligible to receive satellite galaxies if they already have a central.

Once we have specified the number of centrals and satellites in a given halo, we need to give them positions and velocities within the halo. In this ‘vanilla’ HOD model we place the central galaxy at the centre of its halo. We then assign to it the mean velocity of the whole halo, which assumes that it is at rest relative to the halo. For the satellites, we choose their positions and velocities to be equal to those of randomly selected dark matter particles within the halo. This assumes that satellite galaxies trace the spatial and velocity distribution of dark matter within their halo.

Though the HOD is a statistical model that allows us to parameterise our ignorance of the detailed physics of galaxy formation, the various features of the HOD do contain information about galaxy formation. For example, the mass

³ The function for generating Poisson random numbers in ‘Numerical Recipes in C’ code suffers from a floating underflow bug that sets in when N_{sat} exceeds 708 – as can happen for faint samples. We used the ‘GSL’ routine which does not suffer from that particular bug.

² log refers to \log_{10} everywhere in the text

scale and scatter of the central galaxy occupation at low masses (parameterised by M_{\min} and $\sigma_{\log M}$) depend on the luminosity-mass relation in the vicinity of the luminosity threshold of the sample. The luminosity-mass relation depends on the efficiency with which halos are able to cool gas and form stars as a function of mass. This efficiency is affected by several factors, such as supernova feedback, pre-heating caused by reionization, cold versus hot accretion of gas into the halo, merger history, environment, etc. On the other hand, the satellite occupation at higher masses depends primarily on the balance between the accretion and destruction of subhalos, which depends on the distributions of their infall times, masses and orbits, and on the physics of dynamical friction and tidal stripping (e.g., Watson et al. 2011).

To summarise, the vanilla HOD model we use contains five free parameters that control the mean number of galaxies as a function of halo mass: M_{\min} , $\sigma_{\log M}$, M_0 , M_1 , and α . The vanilla model also makes the following set of simplifying assumptions:

1. All galaxies live inside dark matter halos, using whatever halo definition we have adopted.
2. The number of galaxies in a halo only depends on the mass of the halo and not on other halo properties, such as age or concentration. In other words, there is no galaxy assembly bias.
3. The functional forms of $\langle N_{\text{cen}} \rangle$ and $\langle N_{\text{sat}} \rangle$ are given by equation (2) and equation (3).
4. The probability distribution $P(N_{\text{sat}} | \langle N_{\text{sat}} \rangle)$ of the number of satellite galaxies N_{sat} given the mean number $\langle N_{\text{sat}} \rangle$ is a Poisson distribution.
5. The central galaxy in each halo lives at the halo centre and moves with the mean halo velocity. In other words, there is no central spatial or velocity bias.
6. Satellite galaxies in each halo trace the spatial and velocity distribution of dark matter within the halo. In other words, there is no satellite spatial or velocity bias.

These assumptions are all correct to first order; however, most of them are likely incorrect in detail. For example, galaxy assembly bias is usually considered for colour-selected samples, but it is probably also present to some degree for luminosity threshold samples (e.g., Zentner et al. 2014, 2016). We assume that the scatter in N_{sat} at fixed mass is Poissonian. However, recent work with high-resolution N-body simulations suggests that, at least for subhalos, this assumption does not hold for all host-to-satellite mass ratios (Boylan-Kolchin et al. 2010; Mao et al. 2015). Finally, we assume that there is no spatial or velocity bias for centrals or satellites. However, in theory we expect some bias for satellites since they experience dynamical effects (friction and stripping) that do not affect individual dark matter particles. Moreover, there is some observational evidence that both centrals and satellites have some degree of velocity bias (van den Bosch et al. 2005; Guo et al. 2015c). These are the sorts of interesting second-order features of the HOD that can only be probed with an accurate modelling framework like the one we present in this paper. In this first work, we adopt the simple vanilla HOD model to test whether it can be ruled out by SDSS galaxy clustering data. Our strategy for future work is to add freedom to the model as demanded by the data. For example, if the vanilla HOD model is ruled out, then we will be justified to add freedom to it by relaxing

the assumptions described above. If the model is not ruled out, then we will keep adding new clustering statistics until it is. Combining multiple statistics is a clear way forward to break the degeneracies in the HOD model.

3.3 Adding Survey Realism

Once we have a simulation box populated with galaxies according to a given HOD model, we build mock catalogues that contain the main observational systematic effects that plague the galaxy clustering statistics we wish to model, namely redshift space distortions and sample geometry. First, we move the galaxy distribution from Cartesian to spherical coordinates by placing the mock observer at the centre of the simulation cube and converting Cartesian positions of galaxies into RA, DEC, and co-moving distances. We then compute the line-of-sight peculiar velocities of galaxies and compute galaxy redshifts as $1 + z = (1 + z_{\text{cosm}})(1 + z_{\text{doppler}})$, where z_{cosm} is the cosmological redshift and z_{doppler} is the redshift due to the radial peculiar velocity. Finally, we throw out mock galaxies that lie outside the redshift limits or the sky footprint of the SDSS sample. Since the volume of the SDSS sample is much smaller than that of the simulation used to model it, we can extract multiple mock catalogues from a single simulation cube. By applying a series of rotations on the box before converting it to spherical coordinates, we are able to extract four entirely independent mock catalogues from each box. Our 50 simulations for each volume-limited sample can thus produce 200 independent mock catalogues that we can use to construct covariance matrices.

Aside from survey geometry and redshift distortions, the other main source of systematic error present in the SDSS clustering data is incompleteness due to fibre collisions. Unfortunately, adding fibre collisions to our mock catalogues is not a trivial exercise. First, the mocks only represent volume-limited samples, whereas in the SDSS a galaxy can collide with any other galaxy in the full flux-limited sample. Second, the severity of fibre collisions depends on sky location in a complicated way due to the tiling of the survey footprint with spectroscopic plates (Blanton et al. 2003a). In regions where spectroscopic plates overlap, fibre collisions are substantially reduced, and these overlap regions correlate with the surface density of spectroscopic targets. For these reasons, we do not attempt to model fibre collisions, but we simply rely on the nearest-neighbour correction (Zehavi et al. 2002). We then restrict our clustering analysis to regimes where the correction works well, which include scales larger than $0.1h^{-1}\text{Mpc}$ in the correlation function (Zehavi et al. 2002) and groups with at least 5 members in the multiplicity function (Berlind et al. 2006).

4 CLUSTERING MEASUREMENTS

Our approach stems from a very simple and powerful idea: if we have a correct model describing the galaxy distribution, then we should be able to reproduce any clustering statistic that encodes information about the galaxy density field. If the model fails to provide a good fit to clustering statistics, then one or more of its assumptions need revising, e.g., the cosmological model, the halo definition, the

features of the HOD, etc. If the model is able to provide a good fit to some set of clustering statistics, then we can keep adding more statistics until it fails. The galaxy clustering statistics we use do not need to have a physical basis or even be well-established. We could define a new arbitrary statistic and use that instead. Since we can use the same codes and methods to compute statistics on both the data and the model, any statistic that can be measured from the data will do. What we want is statistics that contain a high degree of information about the galaxy density field while still being computationally tractable. In this work we use two fairly traditional statistics, the projected two-point correlation function $w_p(r_p)$ and the group multiplicity function $n(N)$, along with the overall number density of galaxies. In future work, we plan to extend to additional statistics, as well as perform more detailed studies to determine the optimal statistics that should be used for constraining a given model.

4.1 The projected correlation function $w_p(r_p)$

The two-point correlation function is the most widely used galaxy clustering statistic and the one that is typically modelled with HOD models. The three-dimensional correlation function $\xi(r)$ is the excess number of galaxy pairs above what is expected for a random distribution of points, as a function of pair separation r . To deal with redshift distortions, galaxy pairs are decomposed into their line-of-sight and projected components π and r_p , yielding the function $\xi(r_p, \pi)$. This is then integrated over π to get the projected correlation function

$$w_p(r_p) = 2 \int_0^{\pi_{\max}} \xi(r_p, \pi) d\pi. \quad (4)$$

Since we will need to compute clustering statistics on the fly for mock catalogues within our MCMC framework, it is imperative that the computation be fast and efficient. We have developed and used a blazing fast new code `Corrfunc`⁴ (Sinha & Garrison 2017) that can compute $w_p(r_p)$ for either simulation cubes or mock surveys in parallel. With this code we can measure $w_p(r_p)$ out to $20h^{-1}\text{Mpc}$ for 10^6 galaxies in ~ 6 and 3 seconds of wallclock time on a single CPU core, for the number densities of the $M_r < -19$ and -21 samples, respectively.

We use the Zehavi et al. (2002) definitions of r_p and π and we count pairs in 14 equally spaced logarithmic bins of r_p whose centres range from $0.2 - 20h^{-1}\text{Mpc}$. We estimate $\xi(r_p, \pi)$ with the Landy-Szalay estimator ($DD - 2DR + RR$)/ RR (Landy & Szalay 1993), where DD , DR , and RR are the properly normalised numbers of data-data, data-random, and random-random pairs, respectively. We use a random catalogue that contains ~ 10 times more points than its corresponding galaxy sample. Finally, we calculate $w_p(r_p)$ by integrating out to π_{\max} of 40 and $80h^{-1}\text{Mpc}$ for the $M_r < -19$ and -21 samples, respectively. The red points in Fig. 1 show our measurements for the two SDSS samples. Errors are calculated via jackknife resampling using 50 distinct regions on the sky (see McBride et al. 2011 for jackknifing details). These jackknife errors are only used in the

initial steps for constructing a mock covariance matrix, as we describe in § 5. Once we have a mock covariance matrix, we use that for all the main analysis in this paper. Fig. 1 also shows $w_p(r_p)$ for a set of mock catalogues (grey lines and blue points), which we describe in § 5.

We measure $w_p(r_p)$ as described above for the SDSS samples and for the 200 mock catalogues per sample that are used to construct covariance matrices. However, we follow a slightly different approach when computing $w_p(r_p)$ within a HOD parameter search. In this case, we do not use the Landy-Szalay estimator applied to mock catalogues that have the same spherical geometry as the SDSS. Rather, we use the much simpler “natural” estimator $DD/RR - 1$ on full mock cubes that employ the plane parallel approximation, i.e., where one of the axes of the cube serves as the line-of-sight direction. Specifically, we use the single “minimum cosmic variance” box described in § 3.1.2. This methodology is much faster computationally because it does not require a computation of the DR term in Landy-Szalay. Additionally, it does not contain any noise from a random catalogue because in a cubic geometry with periodic boundary conditions the RR term can be calculated analytically. We have verified that this way of computing $w_p(r_p)$ does not introduce any systematic errors in the modelling.

4.2 The Group Multiplicity Function $n(N)$

Galaxy group statistics are naturally well suited to constraining halo models since groups are often systems of galaxies that occupy the same dark matter halo. Berlind & Weinberg (2002) proposed using the group multiplicity function, defined as the abundance of galaxy groups as a function of their richness, to empirically measure the HOD. If galaxy groups are equivalent to halos, then the multiplicity function $n(N)$ is directly related to the probability $P(N|M)$ that a halo of mass M contains N galaxies

$$n(N) = \int_0^\infty \frac{dn}{dM} P(N|M) dM, \quad (5)$$

where dn/dM is the halo mass function. Unfortunately, group catalogues are plagued by severe systematic effects where single halos are split into multiple groups and multiple halos are merged into a single group (e.g., Berlind et al. 2006; Campbell et al. 2015). The measured group multiplicity function is thus very different from the halo multiplicity function given by equation (5). The only way to accurately use group statistics is with a fully numerical modelling procedure where groups are identified directly in mock catalogues and group errors thus affect both data and model equally. Hearin et al. (2013) used the group multiplicity function as measured in mock catalogues to test subhalo abundance matching (SHAM) models and demonstrated that it contains complementary information to the correlation function. However, the multiplicity function has not been used in a full HOD modelling of galaxy survey data because it is computationally difficult to include mock catalogue construction and analysis within the MCMC modelling procedure. This work represents the first such analysis to-date.

We use the Berlind et al. (2006) friends-of-friends algorithm for identifying groups in both SDSS and mock data. According to the algorithm, two galaxies are linked together

⁴ <https://github.com/manodeep/Corrfunc>

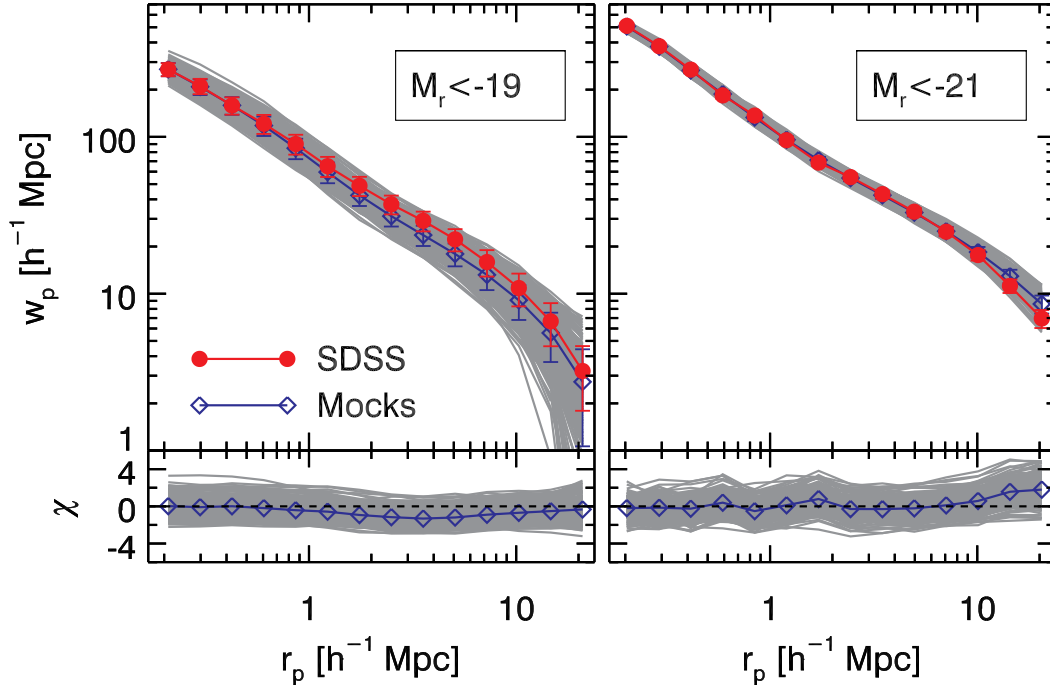


Figure 1. Projected correlation function $w_p(r_p)$ measurements for both SDSS and mock galaxies in the case of the $M_r < -19$ (left panel) and $M_r < -21$ (right panel) samples. Red points show measurements for SDSS galaxies with error bars estimated via jackknife resampling on the sky. Grey lines show individual results for each of 200 mock galaxy catalogues. Blue points and error bars show the mean and standard deviation of $w_p(r_p)$ for the mock catalogues. The bottom section of each panel shows χ , which is the difference between the mock and SDSS measurements divided by the standard deviation of the mocks.

if their projected and line-of-sight separations are both less than a corresponding linking length. A galaxy group then consists of all the galaxies that are linked to each other in this way. We adopt the Berlind et al. (2006) linking lengths of $b_\perp = 0.14$ and $b_\parallel = 0.75$, which are given in units of the mean inter-galaxy separation $n_g^{-1/3}$, where n_g is the sample number density. These linking lengths were specifically optimised to produce a multiplicity function that is as unbiased as possible relative to the true halo multiplicity function. However, this is mostly irrelevant for our study because group finding errors are equally present in both data and model. From our perspective, the group multiplicity function is just a different clustering statistic and any set of linking lengths would work. Using the sample densities listed in Table 1, the co-moving linking lengths for our two SDSS samples are $(r_\perp, r_\parallel) = (0.57, 3.05)h^{-1}\text{Mpc}$ for the $M_r < -19$ sample and $(r_\perp, r_\parallel) = (1.32, 7.06)h^{-1}\text{Mpc}$ for the $M_r < -21$ sample. The co-moving linking lengths that we use on mock samples adjust according to the varying number density.

After running the group finder and generating a group catalogue, we measure $n(N)$ in bins of richness N . For the $M_r < -19$ sample, we adopt the following eight bins of N : (5–6), (7–9), (10–13), (14–19), (20–32), (33–52), (53–84), (85–220). For the $M_r < -21$ sample, we adopt the following six bins of N : (5–6), (7–9), (10–13), (14–19), (20–27), (28–40). $n(N)$ is then simply the co-moving number density of all groups that have a number of members in the range given by each bin. The red points in Fig. 2 show our measurements of the group multiplicity function

for the two SDSS samples. Fig. 2 also shows $n(N)$ for a set of mock catalogues (grey lines and blue points), which we describe in § 5. Unlike in Fig. 1, the displayed error bars on the SDSS measurements are not calculated via jackknife resampling, but rather from the standard deviation of mock measurements.

4.3 The Signal in the Correlation Function

Before we move on to study the covariance matrix of clustering measurements, it is useful to explore where the signal in the galaxy correlation function comes from, in the context of the halo model. In the halo model, the correlation function has two terms, one on small scales that counts pairs of galaxies within the same halo (1-halo) and one on large scales that counts pairs of galaxies in different halos (2-halo). On large scales, the correlation function is simply a weighted version of the correlation function of halos, where halos of a given mass are weighted by the mean number of galaxies for that mass $\langle N \rangle_M$. In this discussion we focus on small scales and we investigate what mass halos dominate the number of galaxy pairs at each physical scale. We do not discuss the sensitivity of ξ to changes in the HOD, which has been presented in other studies (e.g., Berlind & Weinberg 2002; Watson et al. 2011).

The correlation function on small scales depends on the mean number of galaxy pairs per halo mass $\langle N(N-1) \rangle_M$, as well as the spatial distribution of these pairs within halos. Specifically, the 1-halo term of $\xi(r)$ is proportional to

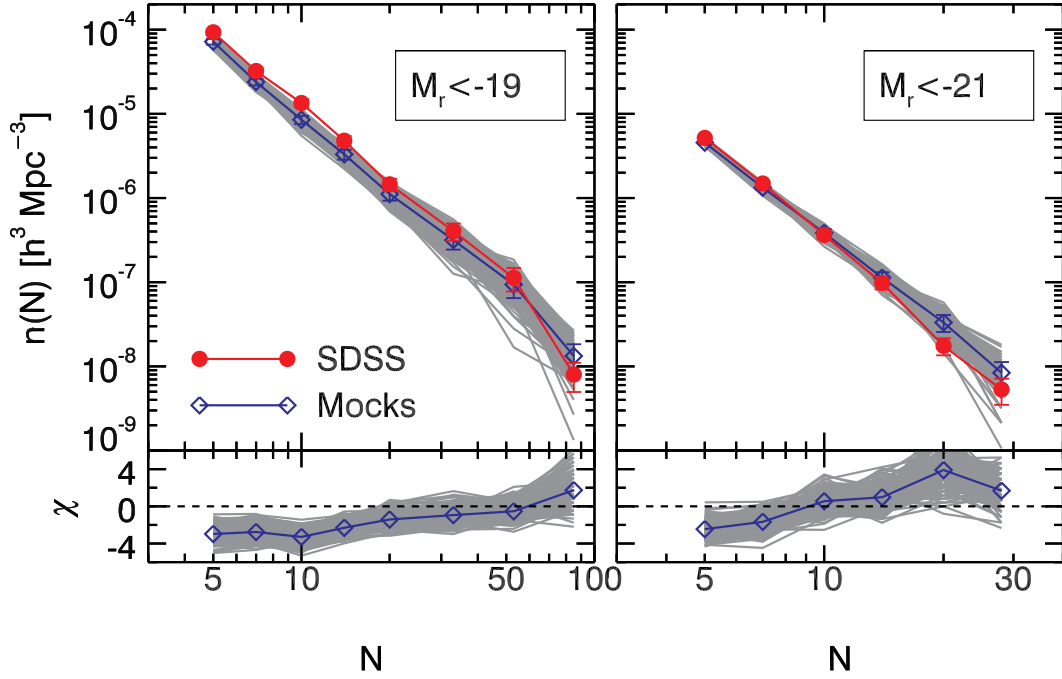


Figure 2. Group multiplicity function $n(N)$ measurements for both SDSS and mock galaxies in the case of the $M_r < -19$ (left panel) and $M_r < -21$ (right panel) samples. Red points show measurements for SDSS galaxies. Grey lines show individual results for each of 200 mock galaxy catalogues. Blue points and error bars show the mean and standard deviation of $n(N)$ for the mock catalogues. Error bars on the red (SDSS) points are estimated from scaling the mock fractional errors to the SDSS measurements. The bottom section of each panel shows χ , which is the difference between the mock and SDSS measurements divided by the standard deviation of the mocks.

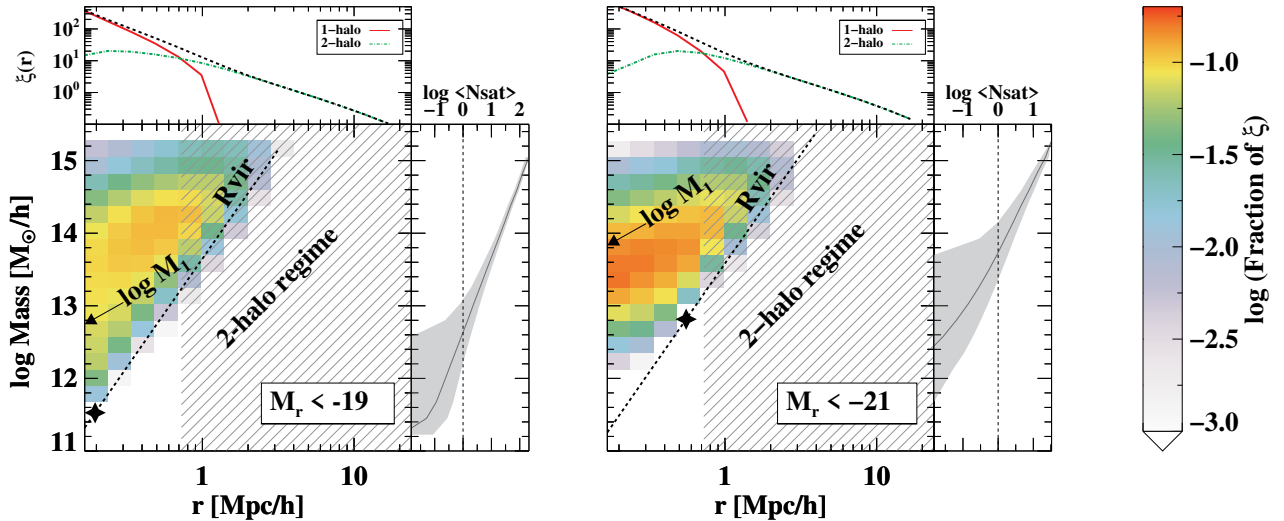


Figure 3. Fractional contribution to 1-halo galaxy pair counts as a function of halo mass and scale in mock catalogues for the $M_r < -19$ (left figure) and $M_r < -21$ (right figure) samples. The main panel for each sample shows two-dimensional bins of scale and halo mass, where the colour of each cell denotes the ratio of the number of 1-halo galaxy pairs in that bin $DD(r, M)$ divided by the number of all 1-halo galaxy pairs at that scale $DD(r)$. Each vertical column of cells thus shows the fractional distribution of halo masses that contribute 1-halo pairs for a particular scale. Also shown in the panel is the value of $\log M_{\min}$ (star symbol), $\log M_1$ (arrow), and the virial radius as a function of mass (dotted line). The hatched region delineates the scales where the 2-halo term dominates the overall clustering signal. The top panel for each sample shows the 1-halo and 2-halo terms of the correlation function $\xi(r)$ separately, while the right panel shows the mean number of satellite galaxies $\langle N_{\text{sat}}(M) \rangle$ (solid line) and its $1\text{-}\sigma$ scatter (shaded region).

(Berlind & Weinberg 2002):

$$r^2 \xi_{1h}(r) \propto \int_0^\infty dM \frac{dn}{dM} \frac{\langle N(N-1) \rangle_M}{2} \frac{F'(r/R_{\text{vir}})}{R_{\text{vir}}(M)}, \quad (6)$$

where dn/dM is the halo mass function, R_{vir} is the virial radius of a halo, and $F'(r)$ is the fractional distribution of galaxy pair separations within a halo. We can determine what mass regime dominates the correlation function by considering how each of the above terms scale with mass. The halo mass function scales as $\sim M^{-1}$ for $M \ll M^*$ and $\sim \exp(-M/M^*)$ for $M \gg M^*$, where M^* is approximately equal to $2 \times 10^{14} h^{-1} M_\odot$.⁵ The mean number of galaxy pairs per halo scales as $\langle N_{\text{sat}} \rangle^2 \sim M^2$ for $M > M_1$. The virial radius scales as $\sim M^{1/3}$. Finally, the spatial distribution function $F'(r/R_{\text{vir}})$ is relatively insensitive to mass. Combining these terms, we find that the total number of pairs contributed from a given mass scales as $\sim M^{2/3}$ for $M \ll M^*$ and $\sim \exp(-M)$ for $M \gg M^*$. As a result, halos of mass M^* should dominate the signal in the 1-halo term of the correlation function and this result should hold for any sample where M_1 is less than M^* .

We next investigate this question in more depth using mock catalogues for our $M_r < -19$ and $M_r < -21$ galaxy samples. Fig. 3 shows the fraction of galaxy 1-halo pairs as a function of mass and scale. In each pixel showing a bin of pair separation r and halo mass M , the colour of the pixel represents the value of $DD(r, M)$, the number of galaxy pairs in that bin, divided by $DD(r)$, the total number of pairs at that scale. In other words, each vertical column of pixels shows the normalised fractional distribution of pair counts as a function of halo mass that contribute to a given scale. The top panel of the figure shows the correlation function $\xi(r)$ with its 1- and 2- halo breakdown, and the right panel shows the mean number of satellite galaxies $\langle N_{\text{sat}}(M) \rangle$. Finally, the figure marks the halo virial radius at each mass, as well as the value of M_1 . Fig. 3 confirms that the majority of galaxy 1-halo pairs come from the cluster regime and that this is true both when M_1 is much lower than M^* (as in the -19 sample), and when M_1 is of order M^* (as in the -21 sample). In the former case each of these clusters contains many satellites and hence several pairs, while in the latter case each cluster only typically contains a single pair. This will help explain the structure of the correlation matrix that we discuss in § 5.2. The halo masses that dominate the 1-halo pairs naturally increase with scale since pairs must fit within the size of the halo.

5 COVARIANCE MATRICES

In order to perform accurate modelling of galaxy clustering measurements, it is not sufficient to have an accurate model; we must also have accurate estimates of the errors on the measurements, as well as the correlations between these errors. In the case of galaxy clustering on small scales, the covariance matrix is typically estimated from the data itself via jackknife resampling using contiguous regions on the sky (e.g., Zehavi et al. 2002). However, jackknife resampling does

not accurately represent cosmic variance since it is limited to the scale of the jackknife subsamples rather than the full size of the galaxy sample. More importantly, Norberg et al. (2009) showed that, even on small scales, jackknife errors are biased in a scale dependent way. A more robust way of estimating the covariance matrix is to use a large number of independent realisations of the full sample, which can be done with mock catalogues.

In addition to the systematic problems with using jackknife errors, there is a more fundamental reason to use mock catalogues for error estimation. When we run a MCMC, we compute a likelihood function that is essentially equal to $P(\text{data}|\text{model})$, the probability that a dataset like the SDSS could be observed given the model being tested. The correct way to estimate this probability is to generate a large number of independent realisations of the model, each of which has the same volume and geometry as the SDSS, and check the fraction of them whose clustering measurements are further from their mean than the SDSS measurements. It is thus more correct to estimate errors from the model being tested than from the observed data set. In other words, the distribution of clustering measurements obtained from realisations of the model is the correct error distribution of the data given the model being tested. For both of these reasons, we use mock catalogues to estimate covariance matrices.

5.1 Methodology

To estimate the covariance matrix of each SDSS sample, we use the 200 independent mock catalogues described in § 3. However, in order to construct the mock catalogues, we need to first choose an HOD model that produces a mock galaxy distribution with similar clustering properties as the SDSS data. This, in turn, requires a covariance matrix. We adopt the following iterative procedure to solve this chicken and egg problem. First, we construct initial covariance matrices for the 1 n_{gal} value and the 14 $w_p(r_p)$ bins of the $M_r < -19$ and -21 samples using jackknife resampling on the sky. Specifically, we use 50 distinct contiguous regions to construct the jackknife samples, as described by McBride et al. (2011). We then use the Nelder & Mead (1965) downhill simplex algorithm to find the best-fit HOD model to our measurements of the projected correlation function. Each time we need to evaluate $w_p(r_p)$ for a given set of trial HOD parameters, we use the ‘‘minimum cosmic variance box’’ as described in § 4.1. We use these best-fit HOD models to construct 200 mock catalogues for each SDSS sample using the methods detailed in § 3.

Fig. 1 and Fig. 2 show the projected correlation functions and group multiplicity functions for each of these mock catalogues (grey lines) as well as the average and standard deviation of the 200 mocks (blue points and error bars). The figures show that the two-point clustering of mock catalogues agrees well with the clustering of the SDSS samples. The group multiplicity function of the mocks roughly agrees with the SDSS, but the agreement is not perfect. This is not surprising given that the multiplicity function was not used in the fit that determined the fiducial mock HOD model. We emphasise that it is not essential that these mocks perfectly match the SDSS clustering; what matters is that the variance among the 200 mocks correctly captures the errors and covariances of our clustering statistics. For this purpose it

⁵ This is not to be confused with the characteristic nonlinear collapse mass in Press-Schechter theory, which is much smaller.

is sufficient to get the clustering approximately right. Fig. 1 shows that the errors estimated from the standard deviation of 200 mocks are approximately in agreement with the errors estimated from jackknife resampling of the SDSS samples on the sky.

Armed with measurements of the global number density n_g , $w_p(r_p)$ and $n(N)$ for each of 200 mocks, we can construct the joint covariance matrix for each of our two samples. The matrices have dimensions 23×23 and 21×21 for the $M_r < -19$ and $M_r < -21$ samples and they are calculated as

$$C_{ij} = \frac{1}{N-1} \sum_1^N (y_i - \bar{y}_i)(y_j - \bar{y}_j), \quad (7)$$

where the sum is over the $N = 200$ mocks, y_i and y_j are two of the measurements (e.g., the number density and one of the multiplicity function bins), and \bar{y}_i and \bar{y}_j are the mean measurements over the 200 mocks. We also compute the correlation matrices, which are simply the covariance matrices normalised by their diagonal elements

$$\mathcal{R}_{ij} = \frac{C_{ij}}{\sqrt{C_{ii}C_{jj}}}. \quad (8)$$

The correlation matrix has values between -1 and 1 , with the diagonal elements being equal to unity by definition.

5.2 The Joint Correlation Matrix

Fig. 4 shows the joint correlation matrix for the $M_r < -19$ sample. The x- and y-axes represent the various bins of the statistics we use – n_{gal} , $w_p(r_p)$ and $n(N)$. The square blocks of cells along the diagonal moving from the bottom left to the top right (1×1 , 14×14 , and 8×8) show the correlation matrices of the individual statistics separately, while the rest of the matrix shows the correlations between different statistics. For example, the first column and bottom row are identical and show the correlation between n_{gal} and all the bins of the other statistics. Fig. 5 shows the same for the $M_r < -21$ sample and differs only in the dimension of the $n(N)$ portion of the matrix, which is 6×6 . The colour of each cell in the matrix denotes the correlation coefficient \mathcal{R}_{ij} , as given by equation (8). Within all the non-diagonal cells, we show the actual measurements from the 200 mock catalogues as black dots. For example, in the second cell of the bottom row of the matrix, the black dots show the scatter plot between n_{gal} and the smallest scale bin of $w_p(r_p)$. These mock data provide a more in-depth way to understand the correlation matrix. Cells where the mock values appear highly correlated (i.e., the black dots resemble a straight line) have \mathcal{R}_{ij} values close to unity, while cells where the mock values seem to be distributed randomly have correlation coefficients close to zero. Since the correlation coefficient \mathcal{R}_{ij} only measures linear trends, it is possible in theory to have a scenario where the two variables are highly correlated (e.g., if they are constrained to be on a circle), but the associated correlation coefficient is zero. However, this is not a concern in this case since the cells with low \mathcal{R}_{ij} shown in Fig. 4 and Fig. 5 do not show any obvious non-linear correlations.

Within the diagonal cells of the correlation matrices shown in Fig 4 and Fig. 5 we display the probability distribution function of each clustering measurement from the 200 mock values (black histograms), along with the best-fit

Gaussian function (white lines). We find that the distribution of mock values is well described by a Gaussian for all the bins in n_{gal} , $w_p(r_p)$, and $n(N)$. Since the error distributions are Gaussian, we can use the χ^2 technique to evaluate the goodness of fit. Finally, in all the cells we have also displayed the SDSS measurements for comparison (white crosses). Since our correlation matrices were created with mocks that were optimised to fit n_{gal} and $w_p(r_p)$, all of the SDSS values for these statistics are consistent with the mock values shown by the black dots. However, we did not optimise the mocks to fit $n(N)$, hence in quite a few of the $n(N)$ cells, the SDSS and mock measurements do not overlap.

Let us now examine the structure in the joint correlation matrices, focusing first on $w_p(r_p)$ and then on $n(N)$. The portions of the correlation matrices that correspond to $w_p(r_p)$ reveal that neighbouring bins are very highly correlated. This is especially true for small scales in the $M_r < -19$ sample, where the first 6 bins contain almost no independent information (they have correlation coefficients greater than 0.9). On larger scales, correlations remain this high, but only for a couple neighbouring bins on each side of a given bin. In general, one must look very far to find bins that exhibit weak correlations. Only the smallest and largest scales of $w_p(r_p)$ that we consider are relatively uncorrelated with each other. The overall degree of correlation is significantly less in the $M_r < -21$ sample, though even there neighbouring couple bins exhibit correlation coefficients higher than 0.8. The largest difference occurs at small scales, where the $M_r < -21$ sample displays much weaker correlations than the $M_r < -19$ sample. These results are in agreement with previous works. In particular, McBride et al. (2011) show their correlation matrices for both the redshift-space and the projected correlation function, revealing that much of the strong correlations on small scales are due to projection. This occurs because each projected scale includes pairs of galaxies from a wide range of physical scales, resulting in a high degree of scale mixing that causes different projected scales to contain very similar information. Even without projection, neighbouring scales in the correlation function are always correlated because they share the same underlying Fourier density modes. The $M_r < -21$ sample displays weaker correlations than the $M_r < -19$ sample for two main reasons. First, it is a lower density sample and thus shot noise, which is inherently uncorrelated, contributes more to the error budget. Second, as we discussed in § 4.3, most 1-halo pairs come from cluster-sized halos in both samples. In the $M_r < -21$ sample these halos typically only contribute a single pair, while in the $M_r < -19$ sample they contribute many pairs each. As the number of clusters fluctuates from mock to mock, in the low luminosity sample these fluctuations will enhance or suppress pairs at all 1-halo scales simultaneously, thus correlating the scales strongly. In the luminous sample this will occur at a much lesser extent.

We next move to the portions of the correlation matrices that correspond to the group multiplicity function, $n(N)$. Different multiplicity bins are not as correlated as different scales of $w_p(r_p)$, but there are still significant correlations (coefficients in the range 0.4-0.8) in the case of the $M_r < -19$ sample. In the $M_r < -21$ sample $n(N)$ correlations are much weaker (coefficients in the range 0.1-0.4). Some of the correlation between bins of $n(N)$ is likely of an indirect nature, due to direct correlations between these

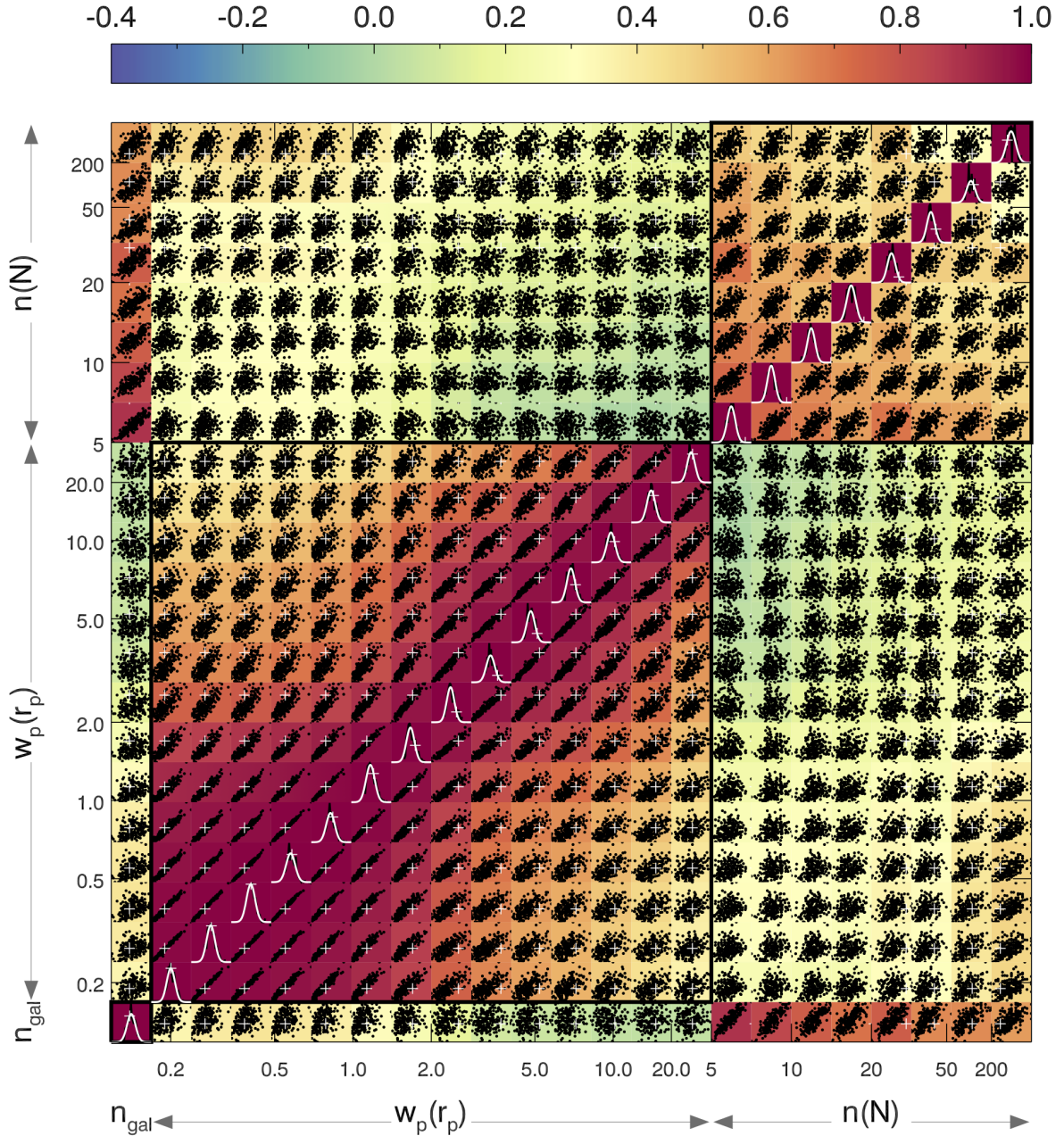


Figure 4. The correlation matrix \mathcal{R} for the number density, n_{gal} (first row/column), projected correlation function, w_p (14 bins), and group multiplicity function, $n(N)$ (8 bins), estimated from 200 independent mock galaxy catalogues of the $M_r < -19$ sample. Each cell shows the correlation between two measurements (for example, the third bin of $w_p(r_p)$ with the second bin of $n(N)$), with the colour of the cell denoting the correlation coefficient as given by equation 8. Also shown within each cell is the corresponding scatter plot of 200 mock values (*black dots*) and the SDSS measurements for comparison (*white cross*). Each diagonal cell shows the distribution of mock values for that measurement (*black histogram*) as well as a Gaussian fit to the distribution (*white line*).

bins and the overall number density n_{gal} , which can be quite strong according to Fig. 4 and Fig. 5. To uncover the intrinsic correlations between the $n(N)$ bins, we subsample the 200 mocks (for both samples) to have identical number densities. We then create new correlation matrices out of these 200 n_{gal} matched mocks. In Fig. 6, we show the original (top panels) and subsampled (bottom panels) joint correlation matrices for the $M_r < -19$ (left panels) and $M_r < -21$ (right panels) samples. The correlation matrices of $w_p(r_p)$ do

not change because the correlation function is not affected by subsampling. However, in both samples we find that, when controlling for n_{gal} , the correlation matrix of $n(N)$ becomes much more diagonal. The matrix becomes completely diagonal in the $M_r < -21$ case, while in the $M_r < -19$ case there is some anti-correlation present between low and high multiplicity groups. This anti-correlation is a result of the nature of the group-finder since, in the case of constant density, an above average abundance of high multiplicity groups

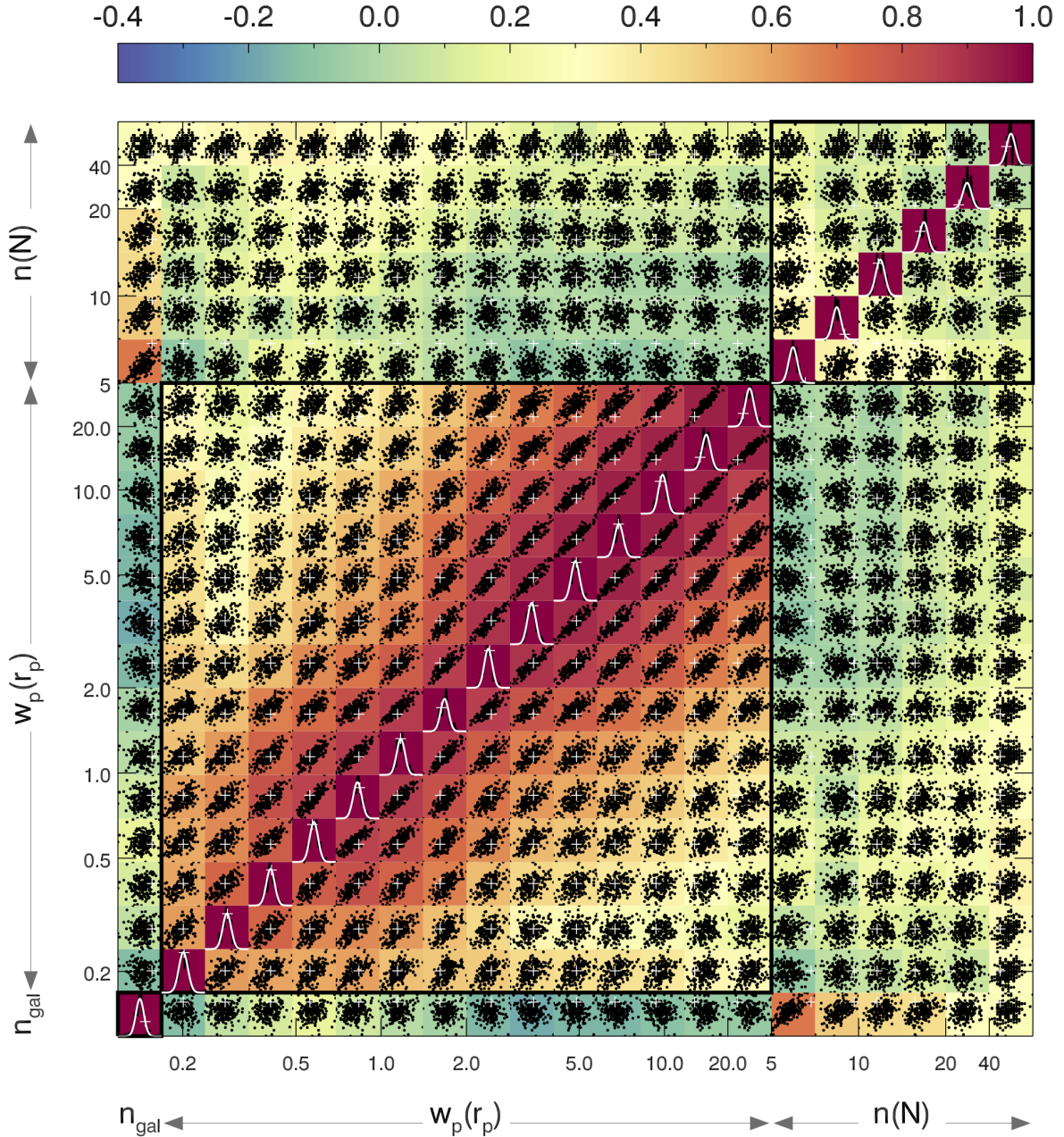


Figure 5. The correlation matrix \mathcal{R} for the number density, n_{gal} (first row/column), projected correlation function, w_p (14 bins), and group multiplicity function, $n(N)$ (6 bins), estimated from 200 independent mock galaxy catalogues of the $M_r < -21$ sample. All features of the plot are the same as in Fig. 4.

in one mock catalogue must come at the expense of low multiplicity groups. From this subsampling test we thus learn that the correlations seen in the group multiplicity function are largely due to correlations with the overall number density. When the density is higher, the entire $n(N)$ is boosted.

5.3 Noise in the Correlation Matrix

Each correlation matrix \mathcal{R} that we have estimated from 200 mock catalogues contains some degree of noise due to the fact that the number of mocks is limited. When we invert the matrix, this noise can amplify and affect the calcula-

tion of χ^2 values in unpredictable ways. We deal with this problem using a singular value decomposition (SVD) approach (e.g., Scoccimarro 2000; Eisenstein & Zaldarriaga 2001; Gaztañaga & Scoccimarro 2005; Norberg et al. 2009). Specifically, we decompose the correlation matrix into its principle components by finding the eigenvectors \mathcal{E}_i and eigenvalues λ_i that satisfy the equations

$$\mathcal{R}\mathcal{E}_i = \lambda_i\mathcal{E}_i. \quad (9)$$

This rotates the space of our measurements into a basis where the eigenvectors are uncorrelated (i.e., where the correlation matrix is diagonal). We can then sort the eigen-

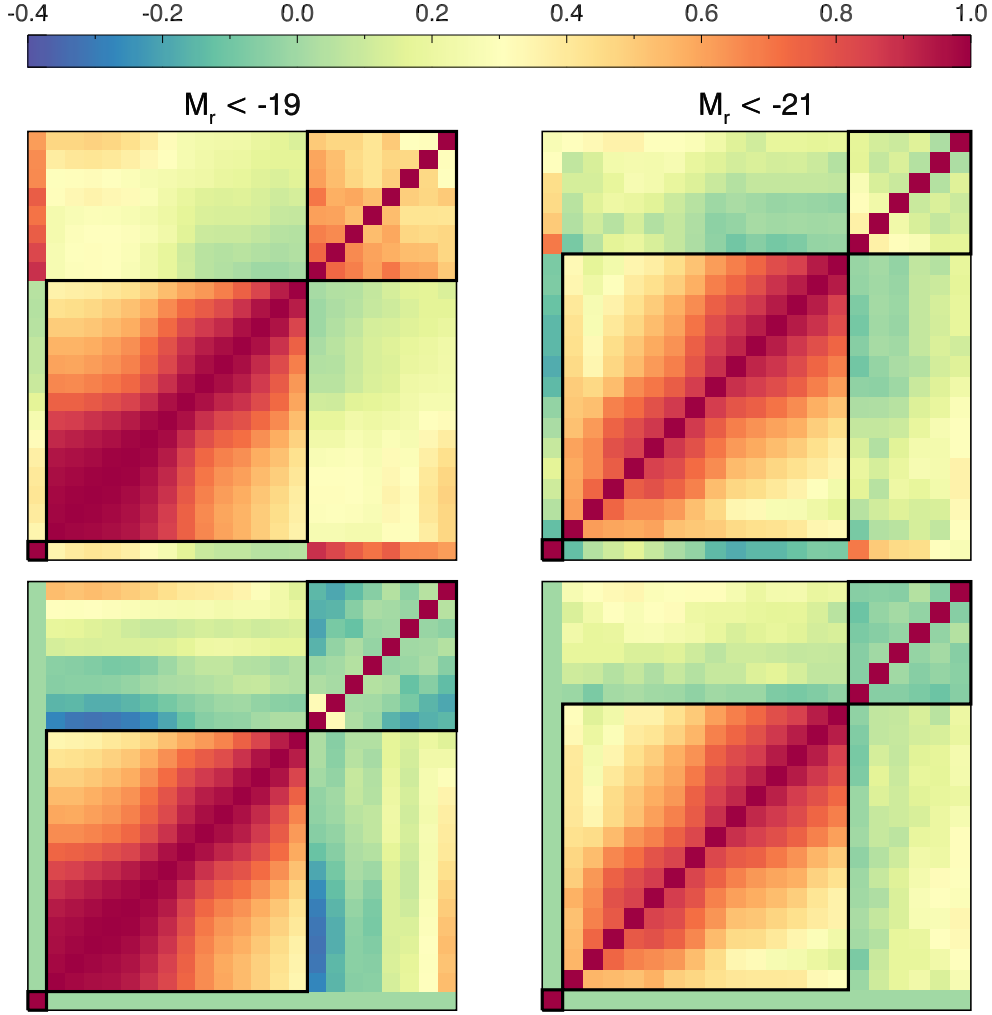


Figure 6. The effect of number density correlations on the correlation matrix for the $M_r < -19$ (left panels) and the $M_r < -21$ (right panels) samples. Top panels show the fiducial correlation matrices as shown in Figs. 4 and 5. Bottom panels show correlation matrices created from the same initial 200 mocks, but after randomly downsampling the mocks to the same galaxy number density, n_{gal} (the lowest amongst the 200 mocks). By matching the n_{gal} in all the mocks, we remove the effect of two measurements showing a correlation due to their individual correlations with n_{gal} . Since the correlation function does not depend on density, randomly downsampling each of the mocks has almost no effect on the correlation coefficients in the $w_p(r_p)$ part of the matrix. However, the correlations in the $n(N)$ bins change drastically. Most of the positive correlations seen in the top panels vanish to reveal nearly diagonal $n(N)$ coefficients in the bottom panels.

vectors by their eigenvalues and trim out those with low eigenvalues, which contain much of the noise, but little information. Following Gaztañaga & Scoccimarro (2005), we only keep eigenvectors for which λ_i^2 is approximately larger than the resolution with which \mathcal{R} is measured, which is

$$\lambda_i^2 \gtrsim \sqrt{\frac{2}{N_{\text{mocks}}}}, \quad (10)$$

where, in our case, $N_{\text{mocks}} = 200$. This procedure effectively reduces the number of data points that we use for fitting models. For the $M_r < -19$ correlation matrix, we trim 12 of the 23 eigenvectors and thus only keep 11 data points in the new orthogonal measurement space. For the $M_r < -21$ matrix, we only trim 5 of the 21 eigenvectors and thus keep 16 data points. The more drastic trimming for the low luminosity sample is a direct result of the higher amount

of correlation present in its correlation matrix. For all the joint fits to n_{gal} , $w_p(r_p)$, and $n(N)$ that we perform and describe in the next section, we run two versions: one with the full correlation matrix and one after trimming out noisy eigenvectors (which we label as PCA in the text). The PCA fits throw away some of the signal present in the data, but the resulting χ^2 values are more reliable and so these are the more conservative results.

6 MODEL FITTING

Our primary objective is to accurately model galaxy clustering statistics and thus test the standard $\Lambda\text{CDM} + \text{halo}$ model. To do this, we explore the HOD parameter space using a MCMC method.

6.1 Computing the Likelihood Function

For each parameter combination we compute the likelihood function $P(\text{data}|\text{model})$. Since the error distributions are Gaussian, the likelihood function is proportional to $\exp(-\chi^2/2)$. We compute the χ^2 statistic as follows

$$\chi^2 = \sum_{ij} \chi_i \mathcal{R}_{ij}^{-1} \chi_j, \quad (11)$$

where \mathcal{R}^{-1} is the inverted correlation matrix and

$$\chi_i = \frac{D_i - M_i}{\sigma_i}, \quad (12)$$

where D_i is the SDSS measurement for data point i , M_i is the model prediction for that measurement, and σ_i is the error in the SDSS measurement. When we use the PCA analysis to reduce noise introduced by inverting the correlation matrix, we calculate χ^2 differently. Since the resulting eigenvectors are uncorrelated, χ^2 is simply a sum of the χ_i^2 contributions for the eigenvectors we have kept (where D_i and M_i are recomputed for the new orthogonal space).

Ideally, each time we moved to a new point in the HOD parameter space, we would compute χ^2 using updated values of σ_i and an updated matrix \mathcal{R} that were generated from the new model. In other words, we would have to create a new set of 200 mock catalogues. This would increase the computational requirement of the MCMC chain by two orders of magnitude and is currently unfeasible. We thus make the approximation that our fiducial HOD, which reproduces the $w_p(r_p)$ measured in the SDSS sample, is representative of the errors and correlation matrix in the parameter-space of interest. Specifically, we adopt the fractional errors given by the fiducial mock catalogues and scale them by the SDSS measurements D_i to obtain

$$\sigma_i = \frac{\sigma_{\text{mock},i}}{M_{\text{mock},i}} \times D_i, \quad (13)$$

where $M_{\text{mock},i}$ and $\sigma_{\text{mock},i}$ are the mean and standard deviation of data point i , as measured from our 200 fiducial mock catalogues. σ_i are then the scaled SDSS errors that we use when computing χ^2 in equation (12).

Given that we fix \mathcal{R} and σ_i using the fiducial mocks, the only ingredient we must compute for each parameter combination within the MCMC is the model prediction M_i . As was discussed in § 3.1.2, we use a substantially larger volume to compute M_i than the SDSS volume that was used to compute D_i . For $w_p(r_p)$, we use a single mock catalogue made from a whole simulation cube, which has approximately 13 times more volume than the corresponding SDSS sample. For $n(N)$ we use the mean of eight mock catalogues, each of which has the same volume as the corresponding SDSS sample. Furthermore, we reduce cosmic variance errors by an additional factor of ~ 2 by carefully selecting which simulation boxes we use to compute M_i . The uncertainties in the model prediction M_i are thus sub-dominant compared to the uncertainties in D_i and we can safely ignore them when we compute the model likelihood.

6.2 Running and Analyzing the MCMC Chains

For each new set of HOD parameters, we must perform the following operations: (1) populate the halo catalogues from two simulation boxes with galaxies according to the HOD;

(2) compute $w_p(r_p)$ on one of these boxes; (3) create eight SDSS-like mock catalogues from the two boxes; (4) run the friends-of-friends group finder on these eight mocks and measure the mean $n(N)$. The codes used for these operations are heavily optimised and take approximately 15 seconds of wallclock time on a single TACC Stampede compute core (for details on the software implementation of $w_p(r_p)$, see Sinha & Garrison 2017). Though this is remarkably fast given the computations involved, it is slow enough that we need to use an efficient and parallel MCMC algorithm to perform the $\sim 10^5$ evaluations of model likelihood required for each parameter search.

We use the code `emcee` (Foreman-Mackey et al. 2013) to generate the MCMC samples. The algorithm employs a number of “walkers” that probe different points in parameter space and can be run in parallel. The MCMC chain is built from a series of iterations where the walkers in each iteration learn from previous iterations and improve their efficiency. We run a total of ten MCMC chains for each luminosity sample. Two of these are model fits to $w_p(r_p)$ or $n(N)$ alone, while the remaining eight are for joint fits to both statistics, using different combinations of assumed cosmology, halo definition, and whether we apply PCA to reduce noise in the correlation matrix (2 cosmological models \times 2 halo definitions \times 2 PCA cases). We note that the number density n_{gal} is explicitly included as a statistic in all chains. For each chain, we use 500 walkers and ~ 1000 iterations for a total of $\sim 500,000$ HOD evaluations. We check for convergence in each parameter by demanding that its probability distribution is stable across iterations and we find that in all cases the chains converge within 200 – 600 iterations.

When running the MCMC, we adopt uniform priors for all five HOD parameters within the following allowed ranges. For the $M_r < -19$ sample, the ranges are $\log M_{\text{min}} : 11 - 12.2$, $\sigma_{\log M} : 0.001 - 1$, $\log M_0 : 6 - 14$, $\log M_1 : 12 - 14$, $\alpha : 0.001 - 2$. For the $M_r < -21$ sample, the ranges are $\log M_{\text{min}} : 12 - 14$, $\sigma_{\log M} : 0.001 - 1$, $\log M_0 : 6 - 15$, $\log M_1 : 13 - 15$, $\alpha : 0.001 - 2$. The motivation for the lower limits on $\log M_{\text{min}}$ and the upper limits on $\sigma_{\log M}$ is to avoid a scenario where we place mock galaxies in halos that are not sufficiently resolved.

When a chain is complete, we throw out the first 200 – 600 iterations since these retain memory of the starting locations of the 500 walkers (the “burn-in” phase). We then explore the posterior probability distribution for each of our five HOD parameters, as well as the joint distributions for different combinations of parameter pairs. We record the median and the percentiles containing 68% of chain values for each parameter and list those as our main marginalised parameter constraints. Moreover, we record the parameter values for the best-fit model, which is simply the point in the whole MCMC chain with the lowest value of χ^2 . To assess goodness-of-fit, we use the p -value that is associated with this best-fit value of χ^2 . The p -value represents the probability that a sample randomly drawn from the best-fit model could have a χ^2 value greater than the one exhibited by the SDSS. In other words, the p -value is the probability that the SDSS is consistent with the best-fit model. Our ability to estimate reliable goodness-of-fit probabilities stems from the fact that we have all the systematic errors of

the analysis under control, and represents one of the main advances of this work.

6.3 Fits to the Correlation Function $w_p(r_p)$

Before modelling the correlation function and the group multiplicity function jointly, we model each statistic alone in order to compare the constraining power of the statistics. First, we model the correlation function measurements together with the number density. This is comparable to what other authors have done in modelling the SDSS DR7 data using both analytic (Zehavi et al. 2011) and mock-based (Zentner et al. 2016) methods. For this analysis we adopt the LasDamas cosmological model and the virial halo definition (Mvir). We also use the original correlation matrices, rather than the PCA versions that have trimmed eigenvectors in order to reduce noise. Since we are only fitting a model to n_{gal} and $w_p(r_p)$, we only use the first 15×15 portion of the correlation matrices shown in Fig. 4 and Fig. 5.

Fig. 7 shows $w_p(r_p)$ for the best-fit model compared to the SDSS data for the two luminosity samples we consider in this work. The error bars in the plot show σ_i as estimated using equation (13). The best-fit model appears by-eye to provide a decent match to the SDSS $w_p(r_p)$. However, visual inspection can be a highly misleading way to assess goodness of fit when data points are highly correlated, as is the case here. We thus rely on values of χ^2 and corresponding p -values. The best-fit values of χ^2 are 14.2 and 19.2 for the $M_r < -19$ and $M_r < -21$ samples, respectively. Both samples have 10 degrees of freedom (14 bins for $w_p(r_p) + 1$ for $n_{\text{gal}} - 5$ free HOD parameters). The resulting p -value for the -19 sample is 0.162, which is acceptable. The p -value for the -21 sample is 0.038, which reveals a tension slightly larger than 2σ , but certainly not enough to warrant ruling out the model. It is notable that the low luminosity sample shows the best goodness-of-fit even though it looks like a worse fit by visual inspection of Fig. 7. This is due to the high degree of correlation between bins in the -19 measurement of $w_p(r_p)$.

6.4 Fits to the Group Multiplicity Function $n(N)$

We now model the group multiplicity function measurements together with the number density. This is the first time this statistic is being used for HOD modelling of SDSS data. As before, for this analysis we adopt the LasDamas cosmological model, the virial halo definition (Mvir), and the original non-PCA correlation matrices. Since we are only fitting a model to n_{gal} and $n(N)$, we only use a 9×9 subset of the full correlation matrix shown in Fig. 4 and a 7×7 subset of the matrix shown in Fig. 5.

Fig. 8 shows $n(N)$ for the best-fit model compared to the SDSS data for the two luminosity samples we consider in this work. The error bars in the plot show σ_i as estimated using equation (13). The best-fit model appears by-eye to provide a perfect match to the SDSS $n(N)$ and the p -values estimated from the χ^2 values confirm this. The best-fit values of χ^2 are 1.6 and 0.1 for the $M_r < -19$ and $M_r < -21$ samples, respectively. The corresponding number of degrees of freedom for the two samples are 4 and 2 (8 or 6 bins for $n(N) + 1$ for $n_{\text{gal}} - 5$ free HOD parameters). The resulting

p -values are 0.81 and 0.95, which are large enough to suggest that the model has too much freedom. A simpler HOD form with fewer free parameters might be equally successful at reproducing the observed $n(N)$.

Since this is the first time that the group multiplicity function is being used to constrain HOD parameters, it is worth comparing its constraining power to that of the correlation function. In the case of the $M_r < -19$ sample, fitting to $n(N)$ yields similar marginalised uncertainties in $\log M_{\text{min}}$ and $\sigma_{\log M}$ compared to fitting to $w_p(r_p)$, but a 20% smaller uncertainty in $\log M_1$ and a 35% smaller uncertainty in α . In the case of the $M_r < -21$ sample however, fitting to $n(N)$ leads to substantially weaker constraints, with uncertainties in $\log M_{\text{min}}$, $\sigma_{\log M}$, $\log M_1$, and α blowing up by 45-100% compared to $w_p(r_p)$. This difference is partly due to the more correlated nature of $w_p(r_p)$ in the low luminosity sample, which reduces its statistical power compared to the high luminosity sample. Since we are not proposing replacing $w_p(r_p)$ as a statistic to fit to, a more relevant way to assess the value of $n(N)$ is to see how HOD constraints improve when fitting to both statistics compared to $w_p(r_p)$ alone. We investigate this next.

6.5 Joint Fits to Both $w_p(r_p)$ and $n(N)$

In this section, we present results from the MCMC chain that simultaneously fits $w_p(r_p)$, $n(N)$, and the galaxy number density. Once again, for this analysis we adopt the LasDamas cosmological model, the virial halo definition (Mvir), and the original non-PCA correlation matrices (the full correlation matrices shown in Fig. 4 and Fig. 5). In the next sections we will explore a different cosmology and halo definition, as well as the effect of reducing noise in the correlation matrices via PCA.

Fig. 9 shows both statistics for the best-fit model compared to the SDSS data, for the two luminosity samples we consider in this work. It is clear from the figure that jointly fitting $w_p(r_p)$ and $n(N)$ is a significantly more challenging task than fitting each statistic individually. The best-fit model for the $M_r < -19$ sample (top panels) reproduces $w_p(r_p)$ reasonably well, but fails at matching $n(N)$, while the reverse is true for the $M_r < -21$ sample (bottom panels). The corresponding values of χ^2 are 39.6 and 34.6 and the number of degrees of freedom are 18 and 16, respectively. The resulting p -values are 0.0024 and 0.0045, which suggest that the model is ruled out at the $\sim 3\sigma$ level when tested against either luminosity sample. The best-fit model results for this and all subsequent MCMC chains are listed in Table 3.

To better understand the tension between fitting $w_p(r_p)$ and $n(N)$, it is helpful to study the posterior probability distributions for the HOD parameters. Fig. 10 shows joint distributions for central galaxy HOD parameters $\log M_{\text{min}}$ vs. $\sigma_{\log M}$, and satellite parameters $\log M_1$ vs. α . We do not show results for M_0 because it is always very poorly constrained. In each case we compare results when fitting our model to $w_p(r_p)$ only (blue contours), $n(N)$ only (green contours), and both statistics jointly (orange contours). The galaxy number density is also used as a constraint in all cases.

First, let us examine the parameter constraints for the $w_p(r_p)$ and $n(N)$ only chains. In the case of the $M_r < -19$

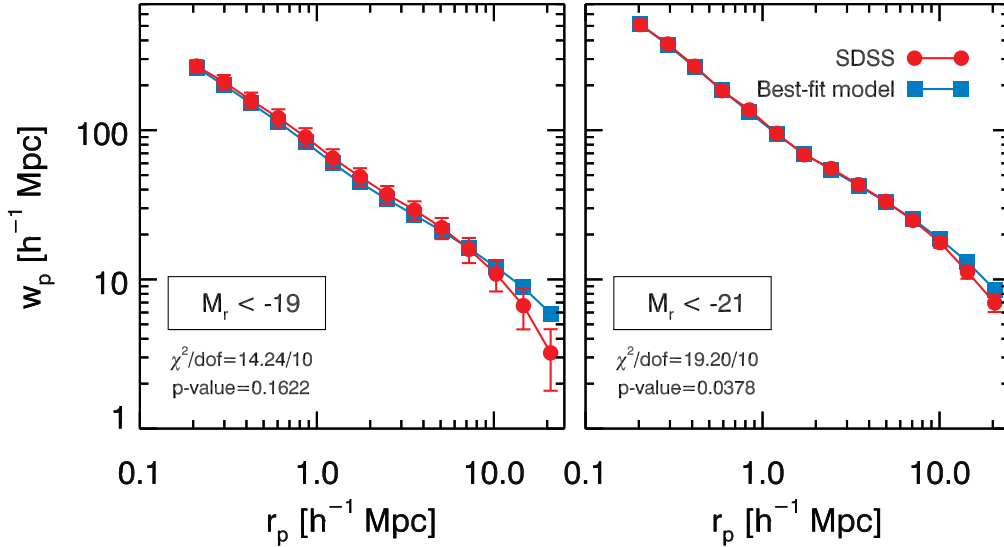


Figure 7. Projected correlation function $w_p(r_p)$ for the best-fit HOD model when the model is only fit to $w_p(r_p)$ and the galaxy number density. Blue points show the best-fit model, while red points show the SDSS measurements in the case of the $M_r < -19$ (left panel) and $M_r < -21$ (right panel) samples. Error bars on the SDSS measurements are estimated from the dispersion among 200 mock catalogues (shown in Fig. 1). The χ^2 , degrees of freedom and p -values are listed in the panels. The model shown here assumes the LasDamas cosmology and the virial halo definition (Mvir) and does not include PCA reduction.

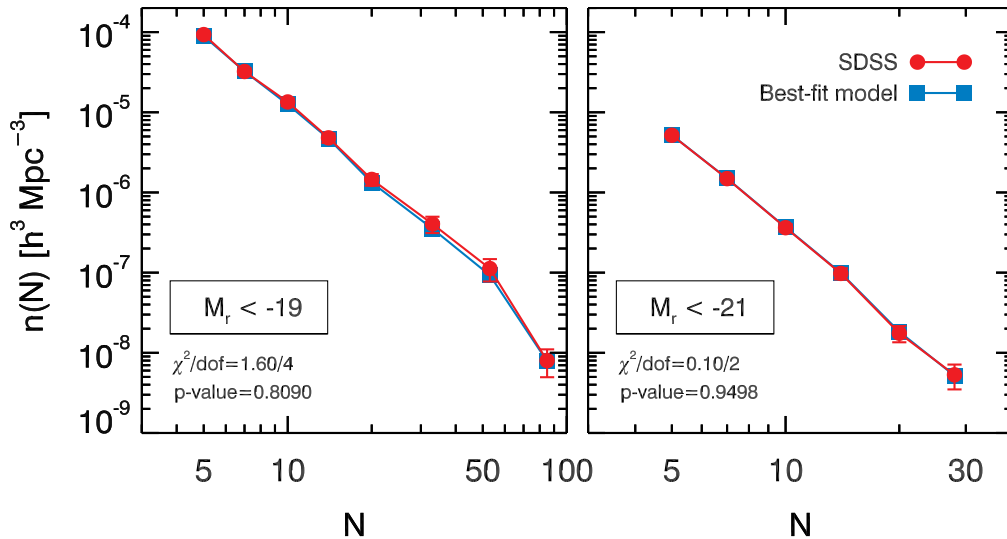


Figure 8. Group multiplicity function $n(N)$ for the best-fit HOD model when the model is only fit to $n(N)$ and the galaxy number density. Blue points show the best-fit model, while red points show the SDSS measurements in the case of the $M_r < -19$ (left panel) and $M_r < -21$ (right panel) samples. Error bars on the SDSS measurements are estimated from the dispersion among 200 mock catalogues (shown in Fig. 2). The χ^2 , degrees of freedom and p -values are listed in the panels. The model shown here assumes the LasDamas cosmology and the virial halo definition (Mvir) and does not include PCA reduction.

sample, the $n(N)$ chain prefers lower values of $\log M_1$ and α , and a higher value of $\log M_{\min}$, compared to the $w_p(r_p)$ chain. To understand this, we can look back at Fig. 2, which shows $n(N)$ for the mock catalogues that we used to make the joint correlation matrices (and that matched the SDSS $w_p(r_p)$ by design). The top panel of that figure shows that the model predictions for $n(N)$ are lower than the SDSS $n(N)$ at all N except for the largest- N bin. In other words, a HOD model that matches the SDSS $w_p(r_p)$ under-predicts $n(N)$ by almost $2\text{-}\sigma$. To fit the SDSS $n(N)$, we would thus need to boost $n(N)$ at all N . This can be achieved primar-

ily by reducing $\log M_1$ (with an adjustment to α). However, reducing $\log M_1$ increases n_{gal} because, in the $M_r < -19$ sample, the satellite fraction is ~ 0.3 so changes in the satellite occupation can contribute a significant change in n_{gal} . This increase in n_{gal} has to be compensated by increasing $\log M_{\min}$ as well.⁶ As a result, the parameter constraints for

⁶ Changing $\log M_{\min}$ only mildly affects $n(N)$ since the linking length changes adaptively as $n_{\text{gal}}^{-1/3}$. The effect is stochastic and affects mostly the small- N groups.

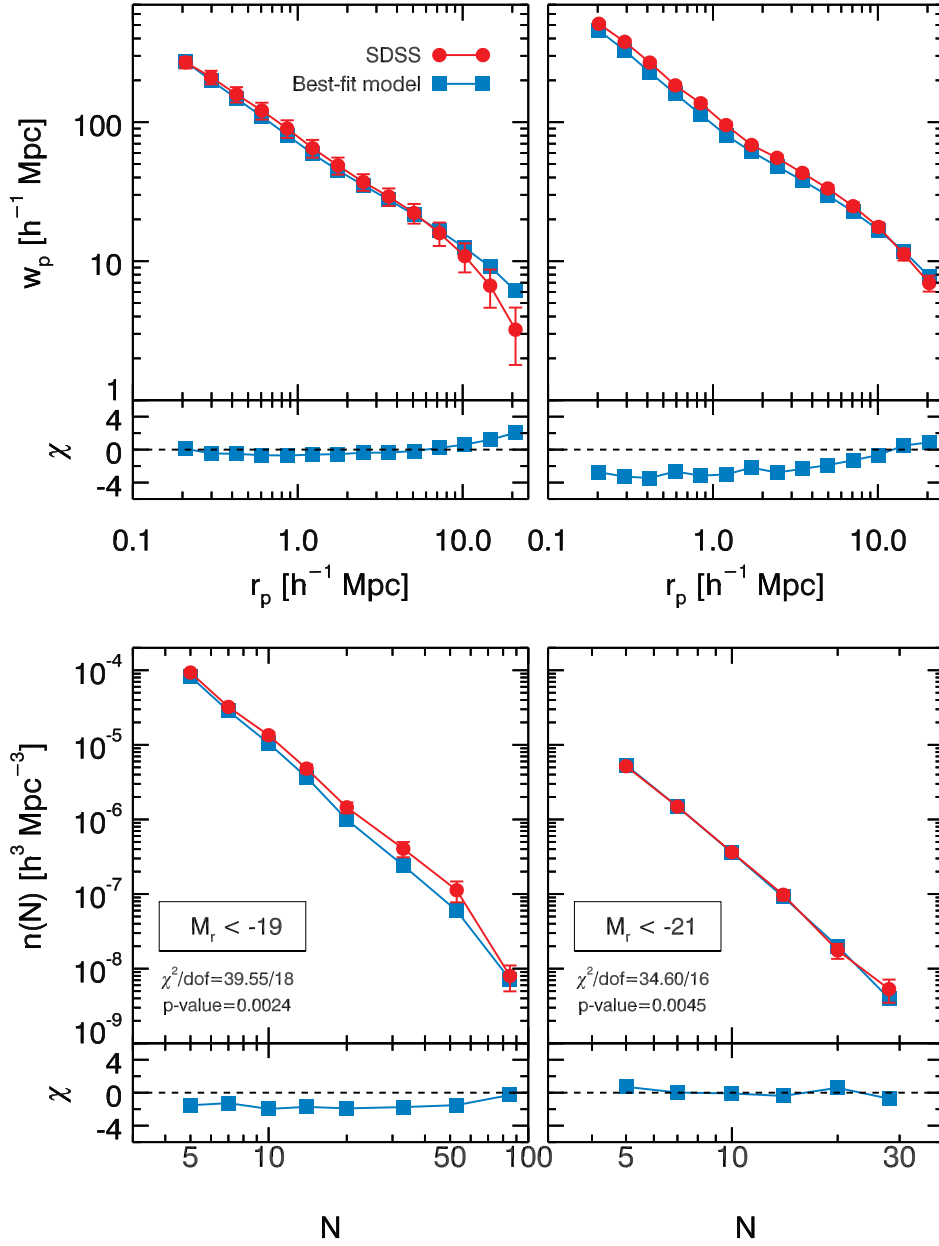


Figure 9. Projected correlation function $w_p(r_p)$ (top panels) and group multiplicity function $n(N)$ (bottom panels) for the best-fit HOD model when the model is jointly fit to $w_p(r_p)$, $n(N)$, and the galaxy number density. Blue points show the best-fit model, while red points show the SDSS measurements in the case of the $M_r < -19$ (left panels) and $M_r < -21$ (right panels) samples. Error bars on the SDSS measurements are estimated from the dispersion among 200 mock catalogues (shown in Figs. 1 and 2). The bottom section of each panel shows χ , which is the difference between the best-fit and SDSS measurements, divided by the standard deviation of the mocks. The χ^2 , degrees of freedom, and p -values are listed in the panels. The model shown here assumes the LasDamas cosmology and the virial halo definition (Mvir) and does not include PCA reduction.

the $n(N)$ only chain have systematically lower $\log M_1$ and higher $\log M_{\min}$ than for the $w_p(r_p)$ only chain.

In the case of the $M_r < -21$ sample, the $n(N)$ chain prefers a somewhat lower value of α , but similar values of the other three parameters, compared to the $w_p(r_p)$ chain. The bottom panel of Fig. 2 shows that the HOD model that matches the SDSS $w_p(r_p)$ predicts a $n(N)$ with a slope that is too shallow (it underpredicts the abundance of small- N groups but overpredicts the abundance of large- N groups). To fit the SDSS $n(N)$, we would thus primarily need to lower

α (with a small adjustment to $\log M_1$). This change to the satellite occupation does not significantly affect n_{gal} because the satellite fraction in the $M_r < -21$ sample is only ~ 0.1 . Consequently, the central galaxy parameters do not need to change.

Fig. 10 shows that the constraints on HOD parameters when fitting jointly to $w_p(r_p)$ and $n(N)$ are significantly tighter than when fitting $w_p(r_p)$ alone. In the case of the $M_r < -19$ sample, adding group statistics reduces the marginalised uncertainties in $\log M_{\min}$, $\sigma_{\log M}$, $\log M_1$,

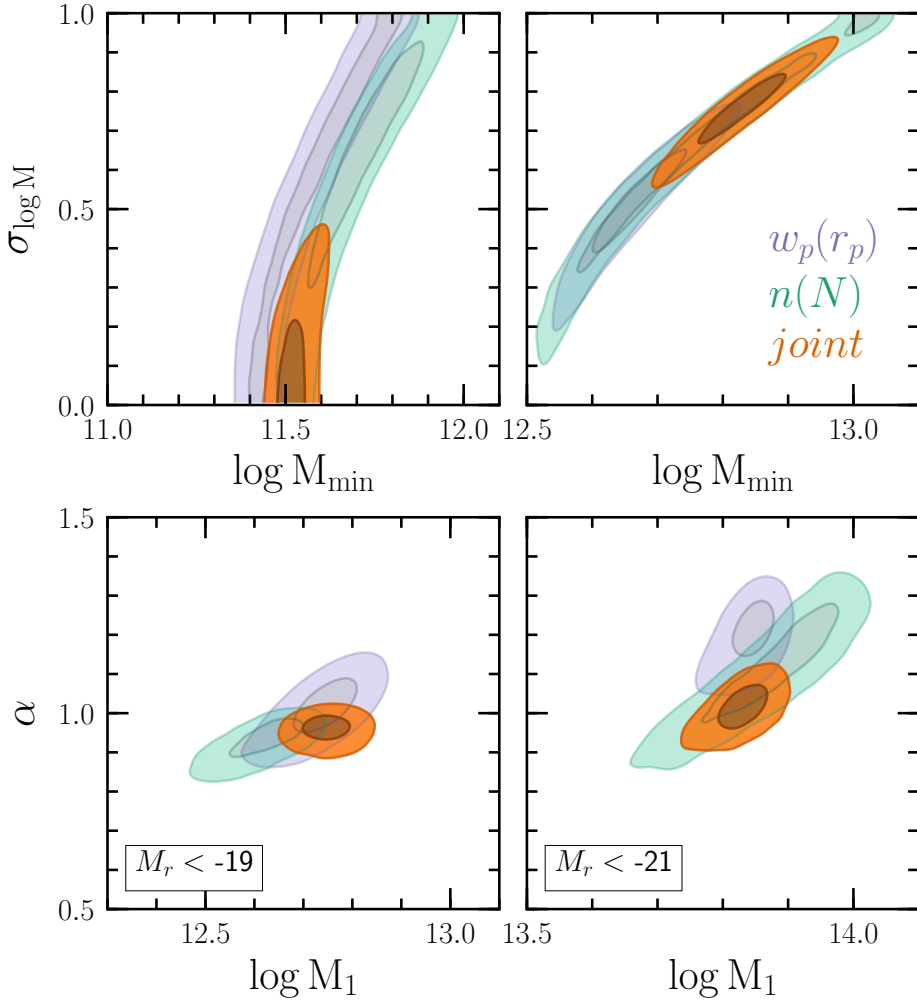


Figure 10. Posterior probability distributions for HOD parameters when the model is fit to SDSS measurements in the case of the $M_r < -19$ (left panels) and $M_r < -21$ (right panels) samples. Top panels show the joint distribution of central galaxy parameters $\log M_{\min}$ and $\sigma_{\log M}$, while bottom panels show the joint distribution of satellite galaxy parameters $\log M_1$ and α . In each case, the probability distributions are marginalised over the remaining three HOD parameters. In each panel, blue, green and orange contours show results when the model is fit to measurements of $w_p(r_p)$ only, $n(N)$ only, and both statistics jointly (together with the galaxy number density in all cases). The contours show the regions of parameter space that contain 68% and 95% of the MCMC probability. The model shown here assumes the LasDamas cosmology and the virial halo definition (Mvir) and does not include PCA reduction.

and α by 40-60%. In the case of the $M_r < -21$ sample, while the uncertainty in $\log M_{\min}$ does not change and the uncertainty in $\log M_1$ only improves by 10%, the uncertainties in $\sigma_{\log M}$ and α improve by 30%. The means and standard deviations of the marginalised posterior distributions for all HOD parameters in this and all subsequent MCMC chains are listed in Table 4. These improved parameter constraints, along with the lower best-fit p -values, demonstrate the power of combining new clustering statistics with $w_p(r_p)$ into HOD modelling of the galaxy distribution.

6.6 Accounting for Noise in the Correlation Matrix

Our results jointly fitting $w_p(r_p)$, $n(N)$, and the galaxy number density of $M_r < -19$ and -20 galaxies with a LasDamas cosmological model, Mvir halos, and the standard 5-parameter HOD, show that the model is ruled out at the

$\sim 3\sigma$ level for both low and high luminosity samples. Before we conclude that our model assumptions are incorrect, we need to make sure that the best-fit p -values are robust. As discussed in § 5.3, noise in our estimated correlation matrices can bias our fit results in difficult to predict ways. We thus follow the PCA procedure outlined in that section to trim noisy eigenvectors from the correlation matrices and we re-run all of our MCMC chains.

Table 3 shows the best-fit results for the PCA chains. In the case of the $M_r < -19$ sample, the best-fit p -value increases by a factor of ~ 30 , from 0.0024 to 0.0751. In other words, the tension between model and data reduces from 3σ to 1.8σ and we no longer rule it out. For the $M_r < -21$ sample, however, the results do not change significantly and the tension between model and data remains strong. The difference between the two samples is due to the much more correlated nature of the low luminosity measurements, as seen in their correlation matrices (Figs 4 and 5). Ta-

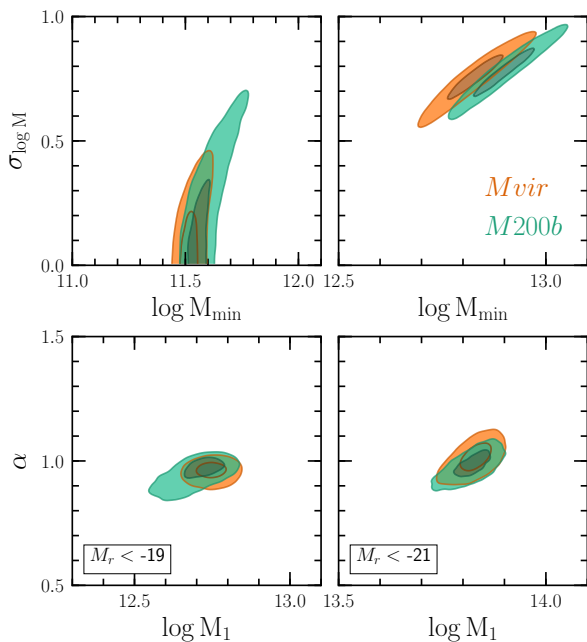


Figure 11. Posterior probability distributions for HOD parameters comparing the cases of two different halo definitions. Panel layout is identical to that in Fig. 10. In each panel, orange and green contours show results for the Mvir and M200b halo definitions, respectively. In both cases, the model shown assumes the LasDamas cosmology and does not include PCA reduction.

ble 4 shows the effect that our PCA analysis has on the HOD parameter constraints. For the $M_r < -19$ sample, the constraints degrade considerably, with 1σ uncertainties in $\log M_{\min}$, $\sigma_{\log M}$, $\log M_1$, and α increasing by factors of 4.3, 2.7, 1.6, and 1.7, respectively. Parameter uncertainties for the $M_r < -21$ sample are unaffected. In summary, the PCA approach leads to no change for the high luminosity sample, and weaker but more reliable constraints for the low luminosity sample. We adopt these as our main results moving forward.

6.7 Varying the Halo Definition and Cosmology

In the halo model framework, the clustering of galaxies is determined by two main ingredients: the halo distribution and the way in which galaxies populate halos, i.e., the HOD. The halo distribution depends on the assumed cosmological model and halo definition. The HOD is comprised of various assumptions, such as the functional form of the mean galaxy occupation, the scatter about the mean, and the spatial and velocity distribution of galaxies within halos. In this section, we probe the sensitivity of our results to the assumed halo definition and cosmological model. Specifically, we introduce a different halo definition (M200b) and different cosmological model (Planck), and we run MCMC chains for all the combinations of these choices. We can then study how sensitive the results are to these assumptions.

First, we consider a change in the halo definition. In principle, any reasonable halo definition should be able to successfully model the galaxy distribution. However, some halo definitions might require more complicated HOD pa-

rameterisations than others. For a given parameterisation (like the 5-parameter model we adopt in this work), some halo definitions likely work better than others. This dependence of HOD modelling on halo definition is a research area that has not been previously explored so the test we perform here represents the first step in that direction.

Our fiducial halo definition, Mvir, corresponds to values of the mean halo over-density (with respect to the mean density) $\Delta = 351$ and 321 for the LasDamas cosmological model at the two median redshifts of the $M_r < -19$ and -21 samples (Bryan & Norman 1998). For the Planck cosmological model that we consider below, the corresponding values are $\Delta = 315$ and 292 . Changing the halo definition to M200b, which corresponds to $\Delta = 200$, makes all halos approximately 20% larger in radius.⁷ As a result, satellite galaxies placed inside halos will be more spatially extended. Moreover, some halos that were previously classified as host halos will now be classified as subhalos, thus changing the probability that they receive a galaxy. These changes will certainly alter $w_p(r_p)$ and perhaps $n(N)$ for a fixed HOD model, but the question is whether a different set of HOD parameters can compensate for this.

Fig. 11 shows posterior probability distributions for HOD parameters for the two halo definitions, when the model is fit jointly to measurements of $w_p(r_p)$, $n(N)$, and n_{gal} . The main effect of changing the halo definition is to shift $\log M_{\min}$ to larger values. This is required to preserve the number density since all halos grow in mass under the M200b definition. The satellite occupation does not change, however. The best-fit results in Table 3 show that adopting this lower Δ definition leads to similar quality fits for the $M_r < -19$ sample (p -value decreases from 0.0751 to 0.0653), but substantially worse fits for the $M_r < -21$ sample (p -value decreases from 0.0056 to 0.0017). Therefore, lowering Δ from the Mvir definition does not alleviate the tension between model and data that we find here.

Next, we consider a change in the cosmological model. Since cosmology and the HOD are not degenerate (Zheng & Weinberg 2007), it is possible that some models work better than others. We compare our LasDamas model to the Planck model. The primary difference between the two is that Planck has a higher value of Ω_m (0.302 vs. 0.25), but there are also differences in Ω_b and n_s . Fig. 12 shows posterior probability distributions of HOD parameters for the two cosmologies, when the model is fit jointly to measurements of $w_p(r_p)$, $n(N)$, and n_{gal} (assuming the Mvir halo definition). The main effect of adopting the Planck cosmology is to shift the whole mean galaxy occupation to higher mass (i.e., increase both $\log M_{\min}$ and $\log M_1$). This shift compensates for the higher halo masses due to the larger value of Ω_m . Table 3 reveals that all the fits improve considerably with the Planck cosmology. In the case of the $M_r < -19$ sample, the p -value shows a modest increase from 0.0751 to 0.1087. However, in the case of the $M_r < -21$ sample, the p -value grows from 0.0056 to 0.0229.

While changing the halo definition did not relieve the tension between model and data, changing the cosmological model does just that. The tension in the $M_r < -21$

⁷ This calculation assumes the Navarro et al. (1997, NFW) density profile.

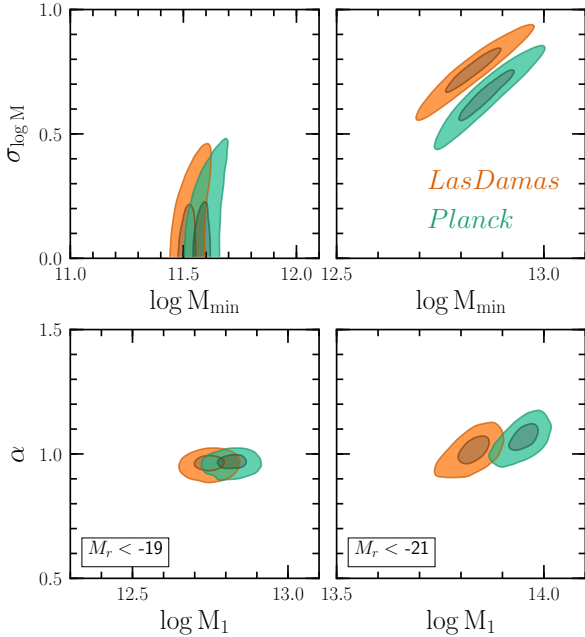


Figure 12. Posterior probability distributions for HOD parameters comparing the cases of two different cosmological models. Panel layout is identical to that in Fig. 10. In each panel, orange and green contours show results for the LasDamas and Planck cosmological models, respectively. In both cases, the model shown assumes the Mvir halo definition and does not include PCA reduction.

sample when adopting the Planck model and the Mvir definition reduces to the 2.3σ level, which is not high enough to warrant ruling the model out. This sensitivity of χ^2 to the assumed cosmology illustrates the power of small-scale clustering to constrain cosmological models. Unfortunately, to properly probe the cosmological parameter space would require a very large number of simulations and is not a trivial exercise.

Looking at all the (PCA) chain results in Table 3, we see that the model that works best for both luminosity samples is the Planck Mvir model. This model combined with the “vanilla” HOD model described in § 3.2 predicts $w_p(r_p)$, $n(N)$, and n_{gal} that are consistent with SDSS measurements for low luminosity galaxies, but show 2.3σ tension for high luminosity galaxies. To further alleviate this tension we would likely have to relax some of the assumptions built into the HOD model. However, the most important result of this paper is that we have achieved a sufficiently robust modelling methodology that we can now test halo models in a statistical sense.

7 FUTURE MODELLING IMPROVEMENTS

In this section we discuss improvements to our modelling pipeline that we leave for future work. Improvements come in two types: changes that reduce systematic errors and thus make the modelling more accurate, and changes that add freedom to the model being tested. Regarding improvements to the model accuracy, we believe that our methodology represents the most accurate HOD modelling to-date given that we compute statistics from realistic mock catalogues,

we compute covariance matrices from a large ensemble of mocks, we account for noise in the matrices, etc. Nevertheless, there are three potential sources of systematic error that need further testing.

First, we do not include fibre collision incompleteness in our modelling pipeline. We apply the nearest neighbour correction to the SDSS data, but we do not attempt to model how this correction might fail. We have argued that, for the scales in $w_p(r_p)$ and multiplicities in $n(N)$ that we consider in this paper, this is sufficient. However, a proper modelling of fibre collisions may become necessary if we extend the analysis to different scales or statistics. Including fibre collisions in the mocks is non-trivial because doing it correctly requires mocks of the full flux-limited SDSS sample. However, it may be possible to approximate the effect with our existing simulations via semi-analytic methods.

Second, the resolution of the simulations that we use to construct the covariance matrix of the $M_r < -21$ sample is fairly low. We expect that this will not have a large impact on the scatter among many simulation realisations, but this needs to be tested more thoroughly. Ideally, we need a proper convergence test, but that would require a very large number of additional simulations (50 boxes per resolution tested). More realistically, we could use fewer mock catalogues of smaller volume each to get a feel for how the covariance matrix depends on resolution.

Third, we construct the correlation matrix from a fiducial HOD model and assume that it is fixed as we explore the HOD parameter space. Ideally, to estimate $P(\text{data}|\text{model})$, we should be recomputing the correlation matrix at each new point in parameter space. This is prohibitively expensive because it would require construction and analysis of 200 mocks at each unique link of the MCMC chain, instead of the ~ 10 that we use now. If testing shows that varying the correlation matrix is necessary, we can explore ways to interpolate between a sparse set of matrices within the parameter space.

There are a number of extensions to the “vanilla” HOD model that we plan to implement for the purpose of giving the model more freedom and to probe interesting aspects of the galaxy-halo connection. For example, we can drop the assumption that satellite occupation follows Poisson statistics, which is not necessarily the case (Boylan-Kolchin et al. 2010; Mao et al. 2015). Another extension is to drop the assumption that the central galaxy is at rest at the halo centre and that satellite galaxies trace the spatial and velocity distributions of dark matter within halos. Several studies, both theoretical (e.g., Berlind et al. 2003) and observational (e.g., van den Bosch et al. 2005), have shown that these are not good assumptions. An HOD model with built-in velocity bias for centrals and satellites was recently used by Guo et al. (2015a). Finally, we can drop the assumption that galaxy occupation statistics only depend on halo mass and account for galaxy assembly bias (Croton et al. 2007). Though there are theoretical reasons to expect some level of assembly bias for luminosity threshold samples (e.g., Zentner et al. 2005; Zehavi et al. 2017), there is not yet strong observational evidence for this. To incorporate assembly bias, we could adopt the “decorated HOD” model of Hearin et al. (2016b), which was recently used to model SDSS data by Zentner et al. (2016). Naturally, as we add freedom to the HOD model, we can also add additional clustering statistics. A great ad-

Table 3. Best-fit HOD Model Results. The table lists the best-fit values of the five HOD parameters (columns 5-9) and the corresponding values of χ^2 , number of degrees of freedom and p -values (columns 10-12) for all the combinations of galaxy sample, assumed cosmology, assumed halo definition, and choice of reducing noise in the correlation matrix via PCA (columns 1-4).

Sample	Cosmology	Halo def	PCA	$\log M_{\min}$	$\sigma_{\log M}$	$\log M_0$	$\log M_1$	α	χ^2	d.o.f.	p-value
$M_r < -19$	LasDamas	Mvir	No	11.53	0.13	9.61	12.75	0.97	39.55	18	0.0024
	LasDamas	Mvir	Yes	11.36	0.14	12.25	12.56	0.90	11.46	6	0.0751
	LasDamas	M200b	No	11.53	0.20	11.88	12.61	0.92	36.63	18	0.0059
	LasDamas	M200b	Yes	11.42	0.12	12.25	12.58	0.92	11.85	6	0.0653
	Planck	Mvir	No	11.58	0.05	11.14	12.80	0.95	38.72	18	0.0031
	Planck	Mvir	Yes	11.40	0.12	12.38	12.64	0.92	10.40	6	0.1087
	Planck	M200b	No	11.62	0.28	11.66	12.77	0.96	35.52	18	0.0081
	Planck	M200b	Yes	11.50	0.22	12.17	12.69	0.94	10.74	6	0.0968
$M_r < -21$	LasDamas	Mvir	No	12.82	0.75	8.97	13.83	1.06	34.60	16	0.0045
	LasDamas	Mvir	Yes	12.81	0.72	11.52	13.83	1.03	26.41	11	0.0056
	LasDamas	M200b	No	12.87	0.75	7.51	13.83	1.03	36.64	16	0.0024
	LasDamas	M200b	Yes	12.89	0.76	8.65	13.83	1.02	29.74	11	0.0017
	Planck	Mvir	No	12.91	0.73	10.21	13.93	1.07	28.96	16	0.0242
	Planck	Mvir	Yes	12.83	0.60	9.00	13.97	1.08	22.20	11	0.0229
	Planck	M200b	No	12.87	0.61	11.35	13.96	1.06	30.76	16	0.0144
	Planck	M200b	Yes	12.89	0.64	9.19	13.95	1.07	23.95	11	0.0130

Table 4. Marginalised HOD Parameter Constraints. Similar to Table 3, except that listed HOD values show the median, and the upper and lower limits corresponding to the 84 and 16 percentiles of the parameter values from the MCMC chain.

Sample	Cosmology	Halo def	PCA	$\log M_{\min}$	$\sigma_{\log M}$	$\log M_0$	$\log M_1$	α
$M_r < -19$	LasDamas	Mvir	No	11.53 ^{+0.05} _{-0.04}	0.15 ^{+0.17} _{-0.11}	8.95 ^{+2.05} _{-2.02}	12.75 ^{+0.04} _{-0.05}	0.96 ^{+0.03} _{-0.04}
	LasDamas	Mvir	Yes	11.59 ^{+0.15} _{-0.15}	0.60 ^{+0.30} _{-0.41}	10.78 ^{+1.42} _{-3.24}	12.63 ^{+0.08} _{-0.08}	0.93 ^{+0.05} _{-0.06}
	LasDamas	M200b	No	11.59 ^{+0.09} _{-0.05}	0.24 ^{+0.26} _{-0.17}	10.72 ^{+1.22} _{-3.20}	12.71 ^{+0.06} _{-0.08}	0.96 ^{+0.04} _{-0.06}
	LasDamas	M200b	Yes	11.65 ^{+0.16} _{-0.16}	0.59 ^{+0.30} _{-0.41}	10.74 ^{+1.51} _{-3.22}	12.64 ^{+0.07} _{-0.09}	0.94 ^{+0.04} _{-0.06}
	Planck	Mvir	No	11.60 ^{+0.05} _{-0.04}	0.15 ^{+0.17} _{-0.11}	9.10 ^{+2.01} _{-2.10}	12.82 ^{+0.04} _{-0.05}	0.96 ^{+0.03} _{-0.03}
	Planck	Mvir	Yes	11.64 ^{+0.17} _{-0.18}	0.61 ^{+0.29} _{-0.40}	11.80 ^{+0.75} _{-3.86}	12.68 ^{+0.09} _{-0.12}	0.92 ^{+0.05} _{-0.07}
	Planck	M200b	No	11.63 ^{+0.06} _{-0.04}	0.21 ^{+0.20} _{-0.14}	9.90 ^{+1.86} _{-2.65}	12.79 ^{+0.05} _{-0.05}	0.97 ^{+0.02} _{-0.04}
	Planck	M200b	Yes	11.70 ^{+0.16} _{-0.17}	0.58 ^{+0.32} _{-0.41}	11.09 ^{+1.30} _{-3.51}	12.71 ^{+0.08} _{-0.09}	0.94 ^{+0.04} _{-0.06}
$M_r < -21$	LasDamas	Mvir	No	12.83 ^{+0.07} _{-0.07}	0.76 ^{+0.09} _{-0.09}	9.62 ^{+2.10} _{-2.38}	13.83 ^{+0.04} _{-0.04}	1.01 ^{+0.05} _{-0.06}
	LasDamas	Mvir	Yes	12.80 ^{+0.07} _{-0.06}	0.72 ^{+0.09} _{-0.09}	9.46 ^{+2.19} _{-2.34}	13.84 ^{+0.03} _{-0.04}	1.03 ^{+0.05} _{-0.06}
	LasDamas	M200b	No	12.90 ^{+0.07} _{-0.07}	0.78 ^{+0.09} _{-0.10}	9.42 ^{+2.09} _{-2.28}	13.82 ^{+0.04} _{-0.05}	0.98 ^{+0.05} _{-0.05}
	LasDamas	M200b	Yes	12.86 ^{+0.07} _{-0.07}	0.72 ^{+0.09} _{-0.10}	9.47 ^{+2.09} _{-2.30}	13.85 ^{+0.04} _{-0.04}	1.01 ^{+0.05} _{-0.05}
	Planck	Mvir	No	12.86 ^{+0.07} _{-0.06}	0.66 ^{+0.10} _{-0.10}	9.54 ^{+2.29} _{-2.39}	13.95 ^{+0.03} _{-0.04}	1.06 ^{+0.05} _{-0.06}
	Planck	Mvir	Yes	12.84 ^{+0.07} _{-0.07}	0.61 ^{+0.11} _{-0.12}	9.73 ^{+2.17} _{-2.52}	13.96 ^{+0.03} _{-0.04}	1.08 ^{+0.05} _{-0.06}
	Planck	M200b	No	12.90 ^{+0.07} _{-0.07}	0.66 ^{+0.10} _{-0.11}	9.87 ^{+1.99} _{-2.49}	13.95 ^{+0.03} _{-0.04}	1.05 ^{+0.05} _{-0.05}
	Planck	M200b	Yes	12.89 ^{+0.07} _{-0.07}	0.63 ^{+0.11} _{-0.11}	9.63 ^{+2.15} _{-2.45}	13.96 ^{+0.03} _{-0.04}	1.07 ^{+0.05} _{-0.05}

vantage of our mock-based modelling methodology is that it can easily incorporate new statistics.

8 SUMMARY AND DISCUSSION

In this paper, we have developed an accurate mock-based HOD modelling framework and have applied it to measurements of the projected correlation function $w_p(r_p)$, the group multiplicity function $n(N)$, and the galaxy number density n_{gal} of two luminosity threshold samples in the SDSS

DR7. Features of the modelling framework include (1) construction of realistic mock galaxy catalogues by populating dark matter halos in cosmological N-body simulations with galaxies, and applying redshift distortions and survey selection functions; (2) calculation of model predictions by running the same analysis codes on mock catalogues as on the SDSS data, and averaging over enough mocks so that statistical errors in the model are negligible; (3) estimation of errors and covariances via 200 independent mock catalogues; (4) reduction of noise in the covariance matrices via

an eigenmode analysis; (5) parameter search using the `emcee` MCMC code that includes $\sim 5 \times 10^5$ evaluations of likelihood; (6) new blazing fast analysis codes that make this data-intensive approach feasible.

The specific model we have tested in this paper is the Λ CDM + “vanilla” HOD model, whereby the dark matter halo population is given by cosmological N-body simulations that contain only dark matter, and galaxies are placed within halos according to a simple 5-parameter HOD model (Zheng et al. 2007) that contains no spatial or velocity bias of centrals or satellites and no galaxy assembly bias. We have tested two cosmological models (LasDamas and Planck) and two halo definitions (Mvir and M200b). Our main results are the following.

- The model is successful at fitting either $w_p(r_p)$ or $n(N)$ (plus n_{gal} in both cases) for both luminosity samples. However, the regions of HOD parameter space selected are different depending on which clustering statistic is used. In terms of constraining power, $n(N)$ yields tighter HOD constraints for low luminosity galaxies, while $w_p(r_p)$ is better at constraining parameters for high luminosity galaxies. When all three statistics are used jointly, HOD constraints tighten significantly compared to the common case of only using $w_p(r_p)$ and n_{gal} .

- The model struggles to jointly fit $w_p(r_p)$, $n(N)$, and n_{gal} , demonstrating the power of combining multiple clustering statistics for ruling out models. Adopting a different halo definition does not make a big difference (though Mvir is slightly preferred over M200b), but changing the cosmological model does. When adopting the LasDamas cosmology, the model is ruled out at the 3σ level when tested against either luminosity sample. However, when adopting the Planck cosmology, the model is consistent with the clustering of low luminosity galaxies and exhibits 2.3σ tension with the clustering of high luminosity galaxies.

Most importantly, we have demonstrated that it is possible to use galaxy clustering on small scales to perform sensitive statistical tests of cosmology + halo models. This is made possible by our fully numerical mock-based methodology combined with fast analysis codes and a careful treatment of systematic and statistical errors. Though most halo model analyses in the literature use analytic models, there are a few studies that have adopted mock-based methods like ours. The first such studies modelled the projected correlation function of red galaxies in the the high redshift (White et al. 2011) and low redshift (Parejko et al. 2013) samples of the BOSS survey. Zheng & Guo (2016) developed a numerical method in which halo pairs and particle pairs within halos are measured in a N-body simulation and tabulated as a function of halo mass and separation. The correlation function of galaxies can then be calculated accurately by appropriately weighting these functions by the HOD. This method was applied to the projected and redshift space correlation functions of BOSS and SDSS galaxies in order to constrain the velocity bias of central and satellite galaxies (Guo et al. 2015a,b,c). The downside of this methodology is that it cannot be extended to other statistics beyond pair (or triple) counts, like the group multiplicity function. The most similar modelling methodology to the one we present in this paper was developed as part of the powerful `halotools` software package (Hearin et al. 2016a). This was recently used

by Zentner et al. (2016) to model the clustering of SDSS galaxies with the goal of constraining galaxy assembly bias. Our analysis improves on Zentner et al. (2016) in the following ways. (1) we include the group multiplicity function as a constraint; (2) we directly adopt the spatial and velocity distribution of particles within halos to place satellite galaxies, while they assume a NFW profile and a Gaussian velocity distribution; (3) we use independent mock catalogues to estimate the covariance matrix, while they use Jackknife resampling; (4) we eliminate noise in the covariance matrix via PCA; (5) they adopt a Poisson error on the galaxy number density, which ignores cosmic variance and is only $\sim 0.33\%$, while the correct errors that we obtain from our 200 mock catalogues are 8% and 2.5% for the $M_r < -19$ and -18 samples, respectively. This work therefore represents the most accurate modelling of SDSS galaxies to-date.

Our hope is that with these and future improvements to the accuracy of modelling together with an optimal set of statistics, galaxy clustering on small scales will definitively measure the galaxy-halo connection, including second-order features like assembly bias. Moreover, small scale clustering has the potential to become a standard test of cosmological models. Whether constraints on cosmology can compete with other probes remains to be seen.

9 ACKNOWLEDGEMENTS

We would like to thank the anonymous referee for constructive comments that helped improve the paper. We would also like to thank Adam Szewciw for running some importance sampling tests to make sure our results are not qualitatively affected by the choice of the correlation matrix. We sincerely thank Jeremy Tinker, Frank van den Bosch, Risa Wechsler, David Weinberg, Andrew Zentner, Andrew Hearin, Doug Watson and Zheng Zheng for valuable discussions over the course of this project. We thank Daniel Foreman-Mackey for the `emcee` MCMC software. We thank Qingqing Mao for software to compute FoF halo centres and Matt Becker for sharing `uber-LGadget2` that was used to run the ConsueloHD and CarmenHD simulations. The mock catalogues used in this paper were produced by the LasDamas project (<http://lss.phy.vanderbilt.edu/lasdamas/>); we thank NSF XSEDE for providing the computational resources for LasDamas. MS especially acknowledges the fantastic `largemem` nodes with 1 TB of RAM at Stampede (TACC) without which the MCMC chains could not have been done. Some of the computational facilities used in this project were provided by the Vanderbilt Advanced Computing Center for Research and Education (ACCRe). This project has been supported by the National Science Foundation (NSF) through a Career Award (AST-1151650). Parts of this research were conducted by the Australian Research Council Centre of Excellence for All Sky Astrophysics in 3 Dimensions (ASTRO 3D), through project number CE170100013. This research has made use of NASA’s Astrophysics Data System and has used `python` (<https://www.python.org/>), `numpy` (Van Der Walt et al. 2011), `matplotlib` (Hunter 2007), `GSL` (<http://www.gnu.org/software/gsl/>), `ChainConsumer` (Hinton 2016), and The (Astronomy) Acknowledgment Generator (<http://astrofrog.github.io/acknowledgment-generator/>).

REFERENCES

- Abazajian K., et al., 2005, *AJ*, **129**, 1755
- Abazajian K. N., et al., 2009, *ApJS*, **182**, 543
- Abbas U., et al., 2010, *MNRAS*, **406**, 1306
- Baugh C. M., Benson A. J., Cole S., Frenk C. S., Lacey C. G., 1999, *MNRAS*, **305**, L21
- Behroozi P. S., Wechsler R. H., Wu H.-Y., 2013, *ApJ*, **762**, 109
- Benson A. J., Cole S., Frenk C. S., Baugh C. M., Lacey C. G., 2000, *MNRAS*, **311**, 793
- Berlind A. A., Weinberg D. H., 2002, *ApJ*, **575**, 587
- Berlind A. A., et al., 2003, *ApJ*, **593**, 1
- Berlind A. A., et al., 2006, *ApJS*, **167**, 1
- Beutler F., et al., 2013, *MNRAS*, **429**, 3604
- Blake C., Collister A., Lahav O., 2008, *MNRAS*, **385**, 1257
- Blanton M. R., 2006, *ApJ*, **648**, 268
- Blanton M. R., Lin H., Lupton R. H., Maley F. M., Young N., Zehavi I., Loveday J., 2003a, *AJ*, **125**, 2276
- Blanton M. R., et al., 2003b, *AJ*, **125**, 2348
- Blanton M. R., et al., 2005, *AJ*, **129**, 2562
- Boylan-Kolchin M., Springel V., White S. D. M., Jenkins A., 2010, *MNRAS*, **406**, 896
- Brown M. J. I., et al., 2008, *ApJ*, **682**, 937
- Bryan G. L., Norman M. L., 1998, *ApJ*, **495**, 80
- Bullock J. S., Wechsler R. H., Somerville R. S., 2002, *MNRAS*, **329**, 246
- Cacciato M., van den Bosch F. C., More S., Mo H., Yang X., 2013, *MNRAS*, **430**, 767
- Campbell D., van den Bosch F. C., Hearin A., Padmanabhan N., Berlind A., Mo H. J., Tinker J., Yang X., 2015, *MNRAS*, **452**, 444
- Colless M., et al., 2001, *MNRAS*, **328**, 1039
- Collister A. A., Lahav O., 2005, *MNRAS*, **361**, 415
- Cooray A., 2006, *MNRAS*, **365**, 842
- Cooray A., Sheth R., 2002, *Phys. Rep.*, **372**, 1
- Crocce M., Pueblas S., Scoccimarro R., 2006, *MNRAS*, **373**, 369
- Croton D. J., Gao L., White S. D. M., 2007, *MNRAS*, **374**, 1303
- Cui W., Borgani S., Dolag K., Murante G., Tornatore L., 2012, *MNRAS*, **423**, 2279
- Davis M., Efstathiou G., Frenk C. S., White S. D. M., 1985, *ApJ*, **292**, 371
- Dawson K. S., et al., 2013, *AJ*, **145**, 10
- Eisenstein D. J., Zaldarriaga M., 2001, *ApJ*, **546**, 2
- Eisenstein D. J., et al., 2005, *ApJ*, **633**, 560
- Foreman-Mackey D., Hogg D. W., Lang D., Goodman J., 2013, *PASP*, **125**, 306
- Gardner J. P., Connolly A., McBride C., 2007, in Shaw R. A., Hill F., Bell D. J., eds, *Astronomical Society of the Pacific Conference Series Vol. 376, Astronomical Data Analysis Software and Systems XVI*. p. 69
- Gaztañaga E., Scoccimarro R., 2005, *MNRAS*, **361**, 824
- Guo H., et al., 2014, *MNRAS*, **441**, 2398
- Guo H., et al., 2015a, *MNRAS*, **446**, 578
- Guo H., et al., 2015b, *MNRAS*, **449**, L95
- Guo H., et al., 2015c, *MNRAS*, **453**, 4368
- Guzik J., Seljak U., 2002, *MNRAS*, **335**, 311
- Hamana T., Ouchi M., Shimasaku K., Kayo I., Suto Y., 2004, *MNRAS*, **347**, 813
- Hearin A. P., Zentner A. R., Berlind A. A., Newman J. A., 2013, *MNRAS*, **433**, 659
- Hearin A., et al., 2016a, preprint, ([arXiv:1606.04106](https://arxiv.org/abs/1606.04106))
- Hearin A. P., Zentner A. R., van den Bosch F. C., Campbell D., Tollerud E., 2016b, *MNRAS*, **460**, 2552
- Hinton S. R., 2016, *The Journal of Open Source Software*, **1**, 00045
- Hunter J. D., 2007, *Computing In Science & Engineering*, **9**, 90
- Jing Y. P., Mo H. J., Börner G., 1998, *ApJ*, **494**, 1
- Jones D. H., et al., 2004, *MNRAS*, **355**, 747
- Jose C., Subramanian K., Srianand R., Samui S., 2013, *MNRAS*, **429**, 2333
- Kauffmann G., Nusser A., Steinmetz M., 1997, *MNRAS*, **286**, 795
- Kauffmann G., Colberg J. M., Diaferio A., White S. D. M., 1999, *MNRAS*, **303**, 188
- Kim J.-W., et al., 2014, *MNRAS*, **438**, 825
- Kravtsov A. V., Berlind A. A., Wechsler R. H., Klypin A. A., Gottlöber S., Allgood B., Primack J. R., 2004, *ApJ*, **609**, 35
- Lacey C., Cole S., 1994, *MNRAS*, **271**, 676
- Landy S. D., Szalay A. S., 1993, *ApJ*, **412**, 64
- Leauthaud A., Tinker J., Behroozi P. S., Busha M. T., Wechsler R. H., 2011, *ApJ*, **738**, 45
- Leauthaud A., et al., 2012, *ApJ*, **744**, 159
- Lee K.-S., Giavalisco M., Gnedin O. Y., Somerville R. S., Ferguson H. C., Dickinson M., Ouchi M., 2006, *ApJ*, **642**, 63
- Magliocchetti M., Porciani C., 2003, *MNRAS*, **346**, 186
- Mandelbaum R., Li C., Kauffmann G., White S. D. M., 2009, *MNRAS*, **393**, 377
- Mao Y.-Y., Williamson M., Wechsler R. H., 2015, *ApJ*, **810**, 21
- Marín F., 2011, *ApJ*, **737**, 97
- McBride C., Berlind A., Scoccimarro R., Wechsler R., Busha M., Gardner J., van den Bosch F., 2009, in *American Astronomical Society Meeting Abstracts #213*. p. 425.06
- McBride C. K., Connolly A. J., Gardner J. P., Scranton R., Newman J. A., Scoccimarro R., Zehavi I., Schneider D. P., 2011, *ApJ*, **726**, 13
- More S., van den Bosch F. C., Cacciato M., Mo H. J., Yang X., Li R., 2009, *MNRAS*, **392**, 801
- Moustakas L. A., Somerville R. S., 2002, *ApJ*, **577**, 1
- Narayanan V. K., Berlind A. A., Weinberg D. H., 2000, *ApJ*, **528**, 1
- Navarro J. F., Frenk C. S., White S. D. M., 1997, *ApJ*, **490**, 493
- Nelder J. A., Mead R., 1965, *The Computer Journal*, **7**, 308
- Neyman J., Scott E. L., 1952, *ApJ*, **116**, 144
- Nikoloudakis N., Shanks T., Sawangwit U., 2013, *MNRAS*, **429**, 2032
- Norberg P., Baugh C. M., Gaztañaga E., Croton D. J., 2009, *MNRAS*, **396**, 19
- Parejko J. K., et al., 2013, *MNRAS*, **429**, 98
- Peacock J. A., Smith R. E., 2000, *MNRAS*, **318**, 1144
- Piscionere J. A., Berlind A. A., McBride C. K., Scoccimarro R., 2015, *ApJ*, **806**, 125
- Planck Collaboration et al., 2014, *A&A*, **571**, A16
- Reid B. A., Seo H.-J., Leauthaud A., Tinker J. L., White M., 2015, *MNRAS*, **444**, 476
- Richardson J., Chatterjee S., Zheng Z., Myers A. D., Hickox R., 2013, *ApJ*, **774**, 143
- Scherrer R. J., Bertschinger E., 1991, *ApJ*, **381**, 349
- Scherrer R. J., Weinberg D. H., 1998, *ApJ*, **504**, 607
- Scoccimarro R., 1998, *MNRAS*, **299**, 1097
- Scoccimarro R., 2000, *ApJ*, **544**, 597
- Scoccimarro R., Sheth R. K., Hui B., Jain B., 2001, *ApJ*, **546**, 20
- Seljak U., 2000, *MNRAS*, **318**, 203
- Sinha M., Garrison L., 2017, *Corrfunc: Blazing fast correlation functions on the CPU*, *Astrophysics Source Code Library* (ascl:1703.003)
- Spergel D. N., et al., 2007, *ApJS*, **170**, 377
- Springel V., 2005, *MNRAS*, **364**, 1105
- Strauss M. A., et al., 2002, *AJ*, **124**, 1810
- Tegmark M., et al., 2004, *ApJ*, **606**, 702
- Tinker J. L., Wetzel A. R., 2010, *ApJ*, **719**, 88
- Tinker J. L., Weinberg D. H., Zheng Z., Zehavi I., 2005, *ApJ*, **631**, 41
- Tinker J. L., Wechsler R. H., Zheng Z., 2010, *ApJ*, **709**, 67
- Tinker J. L., Leauthaud A., Bundy K., George M. R., Behroozi P., Massey R., Rhodes J., Wechsler R. H., 2013, *ApJ*, **778**, 93
- Vale A., Ostriker J. P., 2004, *MNRAS*, **353**, 189

- Van Der Walt S., Colbert S. C., Varoquaux G., 2011, *Computing in Science & Engineering*, 13, 22
- Wake D. A., Croom S. M., Sadler E. M., Johnston H. M., 2008, *MNRAS*, 391, 1674
- Wake D. A., et al., 2011, *ApJ*, 728, 46
- Warren M. S., Abazajian K., Holz D. E., Teodoro L., 2006, *ApJ*, 646, 881
- Watson D. F., Berlind A. A., McBride C. K., Masjedi M., 2010, *ApJ*, 709, 115
- Watson D. F., Berlind A. A., Zentner A. R., 2011, *ApJ*, 738, 22
- Watson D. F., Berlind A. A., McBride C. K., Hogg D. W., Jiang T., 2012, *ApJ*, 749, 83
- White M., et al., 2011, *ApJ*, 728, 126
- Yan R., Madgwick D. S., White M., 2003, *ApJ*, 598, 848
- Yang X., Mo H. J., van den Bosch F. C., 2003, *MNRAS*, 339, 1057
- York D. G., et al., 2000, *AJ*, 120, 1579
- Zehavi I., et al., 2002, *ApJ*, 571, 172
- Zehavi I., et al., 2004, *ApJ*, 608, 16
- Zehavi I., et al., 2005, *ApJ*, 630, 1
- Zehavi I., et al., 2011, *ApJ*, 736, 59
- Zehavi I., Contreras S., Padilla N., Smith N. J., Baugh C. M., Norberg P., 2017, preprint, ([arXiv:1706.07871](https://arxiv.org/abs/1706.07871))
- Zentner A. R., Berlind A. A., Bullock J. S., Kravtsov A. V., Wechsler R. H., 2005, *ApJ*, 624, 505
- Zentner A. R., Hearin A. P., van den Bosch F. C., 2014, *MNRAS*, 443, 3044
- Zentner A. R., Hearin A., van den Bosch F. C., Lange J. U., Villarreal A., 2016, preprint, ([arXiv:1606.07817](https://arxiv.org/abs/1606.07817))
- Zheng Z., 2004, *ApJ*, 610, 61
- Zheng Z., Guo H., 2016, *MNRAS*, 458, 4015
- Zheng Z., Weinberg D. H., 2007, *ApJ*, 659, 1
- Zheng Z., et al., 2005, *ApJ*, 633, 791
- Zheng Z., Coil A. L., Zehavi I., 2007, *ApJ*, 667, 760
- Zheng Z., Zehavi I., Eisenstein D. J., Weinberg D. H., Jing Y. P., 2009, *ApJ*, 707, 554
- van den Bosch F. C., Yang X., Mo H. J., 2003, *MNRAS*, 340, 771
- van den Bosch F. C., Weinmann S. M., Yang X., Mo H. J., Li C., Jing Y. P., 2005, *MNRAS*, 361, 1203
- van den Bosch F. C., et al., 2007, *MNRAS*, 376, 841

This paper has been typeset from a $\text{\TeX}/\text{\LaTeX}$ file prepared by the author.